Master's Thesis

Oscillons und Ihre Signaturen während der Reheating-Phase

Oscillons and Their Signatures During Reheating

prepared by

Robin Fynn Diedrichs

from Hann.-Münden

at the Institute for Theoretical Physics

Abstract

Scalar field models that feature a potential, which is shallower than quadratic, typically permit the existence of soliton-like configurations, called oscillons. Models that aim to describe the inflation and reheating phase often feature such potentials. In recent years the interest in oscillons was rekindled after it was shown that they can lead to a distinct signature in the gravitational wave (GW) spectrum and thus enable the possibility to narrow down the range of possible models by measuring said spectrum. Oscillons are typically driven towards a spherical symmetric configuration and according to Birkhoff's theorem, their radiation of GWs is therefore suppressed. The formation process and asymmetries are the main known mechanisms by which they contribute to the overall GW spectrum. This thesis discusses the aspects of performing lattice simulations that incorporate the evolution of GWs. Additionally, the GW spectrum produced during reheating after hilltop inflation with the inflaton coupled to an additional scalar field is investigated, where it is found that this model does not result in any significant features in the GW spectrum. The developed code is publicly available under https://github.com/rofyd/MLE.

Contents

Contents

1. Introduction

Due to the non-linear nature of the field equations that arise in many models of modern particle physics, a resulting generic feature is the existence of stable (or long-lived) and localized configurations of the field that are called solitons. These structures are of importance to the field of cosmology since they are expected to be produced in a variety of models that are proposed to describe the early universe [1–4]. A direct or indirect detection of a soliton would therefore enable us to narrow down the set of possible models. While density perturbations generally always collapse due to gravity and thus also form localized configurations, it has been shown that a wide range of scalar field potentials also leads to fragmentation into spherical solitons, so-called oscillons [5–13]. The conjectured period of inflation, in which the universe underwent exponential growth, is typically realized with a single scalar field. After inflation is completed, it is assumed that a period of so-called reheating followed in which the scalar field oscillates around a minimum in its potential while decaying into the particles of the standard model of particle physics. It is especially during this phase that solitons can be created. Further, it has been shown that the formation process of oscillons can lead to distinct features in the gravitational wave (GW) spectrum [14, 15]. However, in large-scale inflation models, these features are typically at frequencies that are not measurable today [16]. Still, low-scale inflation models that feature oscillons might produce a distinct GW spectrum that is detectable in the near future.

Due to technological advancements in the last decade, it has become more viable to perform lattice simulations that aim to model the dynamics of the inflaton (and additional fields) during the reheating phase and the resulting GWs. However, there seems to be a common trend among researchers to not make their code publicly available. Instead, it is usually said that a modified version of some existing and publicly available code, such as LatticeEasy, is used, but the modifications are barely discussed (see e.g. [15, 17, 18]). The evolution of GWs in the context of reheating is connected with multiple non-trivialities that can, if handled improperly, lead

to drastically wrong results. It was especially shown that using a second-order accurate stencil for the calculation of the Laplacian does in some cases not capture the dynamics of the system correctly. As part of this thesis, I developed new code on the basis of LatticeEasy that is a graphics processing unit (GPU) accelerated by using the Compute Unified Device Architecture (CUDA) platform, which is being developed by Nvidia [19]. Code validation tests are also presented in this thesis.

The structure is as follows: In chapter 2 I will first summarize all prerequisites that are necessary to understand the context in which oscillons occur. Specifically, after discussing scalar fields and GWs, I will shortly summarize inflation and subsequently discuss the reheating phase. After the prerequisites are established, I describe in chapter 3 the general properties of oscillons, which include their profile and the GW spectrum that they produce. In chapter 4 I will tend to the numerical methods by describing the procedure by which the simulations are performed. Note that the more technical details are not in the main text but in the appendix A. In the following chapter 5 I discuss the code validity by comparing obtained results to previously published results. Additionally, I investigate the production of GWs by oscillons in the hilltop model under the condition that the inflaton field is coupled to an additional scalar field. Aspects of this model were previously investigated in [13], but the production of GWs was not explored. The model is such that the second scalar field gets excited by the oscillons after they already formed, thus enabling the oscillons to possibly create additional features in the GW spectrum that are distinguishable from the background. It is however found that these features do not leave a distinguishable imprint on the spectrum.

2. Prerequisites

This chapter will go over the necessary prerequisites to understand the context in which oscillons will later be studied. This includes the general dynamics of a scalar field on an expanding background, the production of GWs, inflation, and reheating.

Unless otherwise stated, I will be working in units such that $\hbar = c = 1$. Mass is measured in units of the Planck mass $m_{\mathrm{pl}} = (8\pi)^{-1/2}$. I will further use the almost positive metric (-,+,+,+). The Fourier transform is given by

$$f(x) = \int \frac{dk^3}{(2\pi)^3} e^{-ikx} f(k).$$

As for subscripts: Greek letters indicate indices running from zero to three, while roman letters run from one to three. Repeated indices are summed over. Bare time is measured in physical units and bare distances are measured in comoving units.

2.1. Scalar fields in curved space-time

2.1.1. General case

The following summary is based on [20]. The action for a scalar field ϕ that is minimally coupled to gravity in $3 + 1$ dimensions is given by

$$S = \int dx^3 \sqrt{-g} \left[\frac{m_{\mathrm{pl}}^2}{2} R - \frac{1}{2} g^{\mu\nu} \partial_\mu \phi \partial_\nu \phi - V(\phi) \right], \tag{2.1.1}$$

with $g_{\mu\nu}$ the metric, g its determinant, R the Ricci scalar and $V(\phi)$ the potential corresponding to the scalar field ϕ. By varying the action with respect to the metric we obtain the usual Einstein equations

$$R_{\mu\nu} - \frac{1}{2} g_{\mu\nu} R = \frac{1}{m_{\mathrm{pl}}^2} T_{\mu\nu}, \tag{2.1.2}$$

where $R_{\mu\nu}$ denotes the Ricci tensor and $T_{\mu\nu}$ the energy-momentum tensor (EMT),

which is given by

$$T_{\mu\nu} = \partial_\mu\phi\partial_\nu\phi - g_{\mu\nu}\left(\frac{1}{2}\partial_\alpha\phi\partial^\alpha\phi + V(\phi)\right). \tag{2.1.3}$$

If the action is instead varied with respect to the scalar field, then we obtain its equation of motion:

$$g_{\mu\nu}\partial^\mu\partial^\nu\phi = \frac{dV}{d\phi} \equiv V'(\phi). \tag{2.1.4}$$

The above equation describes the dynamics of the system to the full extent of general relativity (GR), however, it is in general not practical nor needed to use full GR. In the following section I will therefore discuss the made simplifications.

2.1.2. Scalar fields on FLRW background

In general, it is a good approximation to consider a homogeneous and isotropic universe, meaning that on large scales quantities like matter density do not depend on direction nor position in space. Therefore, assuming that the universe is homogeneous, isotropic, and flat, then the metric in comoving coordinates is given by

$$ds^2 = -dt^2 + a(t)^2(dx^2 + dy^2 + dz^2), \tag{2.1.5}$$

where a denotes the scale factor. This metric is known as the Friedmann–Lemaître–Robertson–Walker (FLRW) metric. Plugging it into the Einstein equations reduces them to the well known Friedmann equations

$$H^2 = \frac{1}{3m_{\mathrm{pl}}^2}\rho, \tag{2.1.6a}$$

$$\frac{\ddot{a}}{a} = -\frac{1}{6m_{\mathrm{pl}}^2}(\rho + 3p), \tag{2.1.6b}$$

where H is the Hubble constant[1], ρ the total energy density and p the total pressure of the universe. In general, we can see from the above equations that the expansion of space is driven by the energy density of its contents. The second equation can be

---

[1]The Hubble constant is not necessarily a constant. It has this name only for historical reasons.

restated as a conservation law:

$$\dot{\rho} = -3H(\rho + p). \tag{2.1.7}$$

Further, the equations of motion for the scalar field also simplify to

$$\ddot{\phi} + 3H\dot{\phi} - \frac{1}{a^2}\nabla^2\phi + V'(\phi) = 0. \tag{2.1.8}$$

Here we see that due to the expansion of space we obtain an additional term proportional to the Hubble constant. In comparison to a classical oscillator, we can identify this as a friction term and it is therefore also referred to as the Hubble friction term. In general, we have $\dot{a} > 0$ and thus $H > 0$, meaning that due to the Hubble friction any scalar field that has a potential that is bounded from below will eventually be driven to its minimum.

It is useful to investigate how small perturbations of the scalar field ϕ evolve on a homogeneous background. For this we can first decompose the scalar field ϕ into $\phi(t, x) = \bar{\phi}(t) + \delta\phi(t, x)$, where the first term denotes the position independent background and the second term denotes the perturbations. Inserting this decomposition into eq. 2.1.8 reveals that the background evolves according to

$$\ddot{\bar{\phi}} + 3H\dot{\bar{\phi}} + V'(\bar{\phi}) = 0, \tag{2.1.9}$$

while the perturbations evolve at linear order according to

$$\delta\ddot{\phi} + 3H\delta\dot{\phi} - \frac{1}{a^2}\nabla^2\delta\phi + V''(\bar{\phi})\delta\phi = 0, \tag{2.1.10}$$

where I used that the derivative of the potential can be written as

$$V'(\phi) = V'(\bar{\phi} + \delta\phi) = V'(\bar{\phi}) + V''(\bar{\phi})\delta\phi + \mathcal{O}(\delta\phi^2). \tag{2.1.11}$$

More insights can be gained by expanding $\delta\phi$ in terms of its Fourier modes, which I will denote by ϕ_k:

$$\phi_k = \int dx^3 e^{ikx}\delta\phi(x), \tag{2.1.12}$$

such that eq. 2.1.10 becomes

$$\ddot{\phi}_k + 3H\dot{\phi}_k + \left(\frac{k^2}{a^2} + V''(\bar{\phi})\right)\phi_k = 0. \tag{2.1.13}$$

It is convenient to study perturbations with the above equation since the Fourier modes decouple at linear order, making their evolution easier to solve. This equation will later be used again when discussing mechanisms that can lead to exponential growth for certain modes.

2.1.3. Linearized gravity

In order to study the production of GWs, it is first necessary to consider small perturbations to the FLRW metric, to then identify the components of the metric perturbation that represent GWs and then derive its equations of motion. The following summary is based on [20–22] and more details about the derivations can therefore be found in these references.

Let $\delta g_{\mu\nu}$ be the perturbation to the flat FLRW metric, then this perturbation can be decomposed into scalar, vector, and tensor components, such that

$$
\begin{aligned}
\delta g_{00} &= -2\phi, \\
\delta g_{0i} &= \delta g_{i0} = \partial_i B + S_i, \\
\delta g_{ij} &= \delta g_{ji} = -2\psi\delta_{ij} + \left(\partial_i\partial_j - \frac{1}{3}\delta_{ij}\nabla^2\right)E + \partial_i F_j + \partial_j F_i + h_{ij},
\end{aligned}
\tag{2.1.14}
$$

with ϕ, B, ψ and E scalar components, S_i and F_i vector components and h_{ij} a tensor component. This decomposition is especially convenient since scalar, vector and tensor components evolve independently from each other at linear order. The components have to further fulfill additional requirements such that

$$
\partial_i S_i = 0, \quad \partial_i F_i = 0, \quad \partial_i h_{ij} = 0, \quad h_{ii} = 0,
\tag{2.1.15}
$$

where the last two conditions guarantee the tensor mode to be transverse and traceless. Note that since h_{ij} has to be symmetric, it could in principle have 6 independent degrees of freedom (dof), however the above constraints reduce this number by 4, meaning that h_{ij} only has 2 dof, which correspond to the two possible polarization modes of GWs.

The Einstein field equations are invariant under infinitesimal coordinate transformations $x_\mu \to x_\mu + \xi_\mu$, with ξ_μ a space-time dependent four-vector. This transformation can be exploited to simplify the metric decomposition to a certain degree. Such a transformation will transform the metric perturbations as $\delta g_{\mu\nu} \to \delta g_{\mu\nu} - \partial_\mu \xi_\nu - \partial_\nu \xi_\mu$.

However, before looking at how the individual components of $\delta g_{\mu\nu}$ transform, it is helpful to first also decompose the vector ξ_μ into scalar and vector components, such that $\xi_\mu = (d_0, \partial_i d + d_i)$ and $\partial_i d_i = 0$, with d_0, d scalar functions and d_i a vector function. While the tensor component is left invariant, scalar components transform as

$$\phi \to \phi + \dot{d}_0, \quad \psi \to \psi + \frac{1}{3}\nabla^2 d, \quad B \to B - d_0 - \dot{d}, \quad E \to E - 2d, \qquad (2.1.16)$$

and the vector components as

$$S_i \to S_i - \dot{d}_i \quad \text{and} \quad F_i \to F_i - d_i. \qquad (2.1.17)$$

In this work, we are only interested in the components of the metric perturbations that represent GWs. It can be shown that only the tensor component inherits radiative degrees of freedom and can therefore be identified as the component representing GWs [20]. It is therefore useful to transform the other components such that the equations of motion for the tensor part become more convenient to solve. For this, I will make use of the synchronous gauge in which ξ_μ is chosen such that $\phi = B = 0$. It is noteworthy that this gauge does not eliminate the entire gauge freedom and can have nonphysical singularities. In the context of this thesis, this is however not necessarily a problem since only the tensor part, which is already gauge invariant, is of interest. Further, vector perturbations decay with the expansion of the universe, and I will therefore not consider them henceforth. We therefore now have

$$
\begin{aligned}
\delta g_{00} &= 0, \\
\delta g_{0i} &= \delta g_{i0} = 0, \\
\delta g_{ij} &= \delta g_{ji} = -2\psi \delta_{ij} + \left(\partial_i \partial_j - \frac{1}{3}\delta_{ij}\nabla^2 \right) E + h_{ij} \equiv S_{ij},
\end{aligned}
\qquad (2.1.18)
$$

where I introduced S_{ij} to explicitly denote δg_{ij} in the synchronous gauge. In general it is always possible to obtain ψ, E and h_{ij} from S_{ij} by applying appropriate projectors. Especially h_{ij} is obtained by projecting S_{ij} to transverse-traceless (TT) space. In Fourier space this projection is given by

$$h_{ij}(k,t) = \Lambda_{ij,lm}(\hat{k}) S_{lm}(k,t), \quad \text{with}$$

$$\Lambda_{ij,lm}(\hat{k}) = P_{il}(\hat{k}) P_{jm}(\hat{k}) - \frac{1}{2} P_{ij}(\hat{k}) P_{lm}(\hat{k}), \quad P_{ij}(\hat{k}) = \delta_{ij} - \hat{k}_i \hat{k}_j, \quad \hat{k} = \frac{k}{|k|}. \tag{2.1.19}$$

In total the metric takes the form of

$$ds^2 = -dt^2 + a(t)^2 (\delta_{ij} + S_{ij}) dx^i dx^j. \tag{2.1.20}$$

Inserting this metric into the field equations 2.1.2 results in the following equations of motion for S_{ij} at linear order

$$\ddot{S}_{ij} + 3H\dot{S}_{ij} - \frac{1}{a^2}\Delta S_{ij} = \frac{2}{m_{\text{pl}}^2 a^2} T_{ij}. \tag{2.1.21}$$

In momentum space this equation is that of a forced oscillator, which is sourced by the EMT. Note that instead of evolving S_{ij}, it would alternatively also be possible to directly evolve h_{ij} by projecting the EMT to TT space and then using it as the source in the above equation. Both methods will, of course, give the same result, the computational cost is however different. The actual equation that will be evolved by the program is later discussed in sec. 4.4.

2.1.4. Gravitational wave spectrum

The 00 component of the EMT for GWs corresponds to their energy. If we consider GWs within in a finite box of comoving volume $\mathcal{V}$ and periodic boundary conditions, then this energy is given by [22]

$$\rho_{\text{gw}}(t) = \frac{m_{\text{pl}}^2}{4} \left\langle \dot{h}_{ij}(x,t) \dot{h}_{ij}(x,t) \right\rangle_{\mathcal{V}}, \tag{2.1.22}$$

where $\langle \dots \rangle_{\mathcal{V}}$ denotes averaging over the volume $\mathcal{V}$. However, we are in general not interested in the spatial distribution of this energy density, but rather in its distribution in momentum space. Inserting the definition of the Fourier transform results in

$$
\begin{aligned}
\rho_{\mathrm{gw}}(t) &= \frac{m_{\mathrm{pl}}^2}{4} \left\langle \dot{h}_{ij}(x,t)\dot{h}_{ij}(x,t)\right\rangle_{\mathcal{V}} \\
&= \frac{m_{\mathrm{pl}}^2}{4}\frac{1}{\mathcal{V}} \int dx^3 \dot{h}_{ij}(x,t)\dot{h}_{ij}(x,t) \\
&= \frac{m_{\mathrm{pl}}^2}{4}\frac{1}{\mathcal{V}}\frac{1}{(2\pi)^6} \int dx^3 \int dk^3 \int dk'^3 e^{i(k'+k)x}\dot{h}_{ij}(k,t)\dot{h}_{ij}(k,t) \\
&= \frac{m_{\mathrm{pl}}^2}{4}\frac{1}{\mathcal{V}}\frac{1}{(2\pi)^3} \int dk^3 \int dk'^3 \delta(k'+k)\dot{h}_{ij}(k,t)\dot{h}_{ij}(k,t) \\
&= \frac{m_{\mathrm{pl}}^2}{4}\frac{1}{\mathcal{V}}\frac{1}{(2\pi)^3} \int dk^3 \dot{h}_{ij}(k,t)\dot{h}_{ij}^*(k,t).
\end{aligned}
\tag{2.1.23}
$$

For cosmological studies, it is usually custom to calculate the gravitational energy per logarithmic frequency interval and normalize the result by the critical density of the universe ρ_{crit}. The former is defined via

$$
\rho_{\mathrm{gw}} = \int_0^\infty \frac{dk}{k} \frac{d\rho_{\mathrm{gw}}}{d\log k},
\tag{2.1.24}
$$

which results in

$$
\begin{aligned}
\frac{d\rho_{\mathrm{gw}}}{d\log k} &= k^3 \frac{m_{\mathrm{pl}}^2}{4}\frac{1}{\mathcal{V}}\frac{1}{(2\pi)^3} \int d\Omega\, \dot{h}_{ij}(k,t)\dot{h}_{ij}^*(k,t) \\
&= k^3 \frac{m_{\mathrm{pl}}^2}{8\pi\mathcal{V}} \left\langle \dot{h}_{ij}(k,t)\dot{h}_{ij}^*(k,t)\right\rangle_\Omega,
\end{aligned}
\tag{2.1.25}
$$

where $d\Omega$ denotes integration over a spherical shell, and $\langle\ldots\rangle_\Omega$ averaging over said shell. The critical density of the universe is given by

$$
\rho_{\mathrm{crit}} = 3m_{\mathrm{pl}}^2 H^2.
\tag{2.1.26}
$$

We, therefore, arrive at

$$
\Omega_{\mathrm{gw}} \equiv \frac{1}{\rho_{\mathrm{crit}}} \frac{d\rho_{\mathrm{gw}}}{d\log k} = \frac{k^3}{24\pi H^2 \mathcal{V}} \left\langle \dot{h}_{ij}(k,t)\dot{h}_{ij}^*(k,t)\right\rangle_\Omega.
\tag{2.1.27}
$$

In addition, it is necessary to redshift the spectrum to today. For this, it is needed to calculate the ratio of the scale factor at the end of the simulation to the scale factor today. From here on I will use subscripts of e to denote quantities at the end of the simulation, $*$ for quantities at the end of reheating, and 0 for quantities at

2. Prerequisites

present time. Then, the needed ratio is given by

$$\frac{a_e}{a_0} = \frac{a_e}{a_*}\frac{a_*}{a_0}. \tag{2.1.28}$$

The second fraction on the right-hand side can be estimated by assuming that the universe is in thermal equilibrium since the end of reheating. In thermal equilibrium the comoving entropy density is constant, such that $g_S T^3 a^3 = \text{const}$, where g_S denotes effective entropic degrees of freedom (see [23] for a full derivation of this quantity). The desired ratio is then given by

$$\frac{a_*}{a_0} = \frac{T_0}{T_*}\left(\frac{g_{S,0}}{g_{S,*}}\right)^{\frac{1}{3}}. \tag{2.1.29}$$

The temperature can further be related to the energy density in radiation, such that $\rho_{\text{rad}} \propto g T^4$, with g denoting relativistic degrees of freedom. The above equation can therefore be restated as

$$\frac{a_*}{a_0} = \left(\frac{\rho_{\text{rad},0}}{\rho_{\text{rad},*}}\right)^{\frac{1}{4}}\left(\frac{g_*}{g_0}\right)^{\frac{1}{4}}\left(\frac{g_{S,0}}{g_{S,*}}\right)^{\frac{1}{3}} = \left(\frac{\rho_{\text{rad},0}}{\rho_{\text{rad},*}}\right)^{\frac{1}{4}}\left(\frac{g_*}{g_0}\right)^{-\frac{1}{12}}, \tag{2.1.30}$$

where in the last step I assumed that $g \approx g_S$. Also, I assume that all energy at the end of the simulation is transferred to radiation, such that $\rho_e = \rho_{\text{rad},e}$. The energy density at the end of reheating can further be related to the energy density at the end of the simulation by assuming that the universe expands according to an effective equation of state parameter w during that period, such that the energy density scales according to $\rho \propto a^{-3(1+w)}$ and therefore

$$\frac{\rho_*}{\rho_e} = \left(\frac{a_*}{a_e}\right)^{-3(1+w)}. \tag{2.1.31}$$

Inserting the above equation together with eq. 2.1.30 into eq. 2.1.28 results in

$$\frac{a_e}{a_0} = \frac{1}{\rho_e^{1/4}}\left(\frac{a_e}{a_*}\right)^{1-\frac{3}{4}(1+w)}\left(\frac{g_*}{g_0}\right)^{-\frac{1}{12}}\rho_{\text{rad},0}^{1/4}. \tag{2.1.32}$$

Since the energy density of GWs scales with $\rho_{\text{GW}} \propto a^{-4}$, we have

$$\rho_{\text{gw},0} = \rho_{\text{gw},e}\left(\frac{a_e}{a_0}\right)^4 = \rho_{\text{gw},e}\frac{1}{\rho_e}\left(\frac{a_e}{a_*}\right)^{1-3w}\left(\frac{g_*}{g_0}\right)^{-\frac{1}{3}}\rho_{\text{rad},0}. \tag{2.1.33}$$

Further, since I assume the universe to be flat we also have $\rho_{\text{crit,e}} = \rho_e$ and therefore

$$\rho_{\text{crit,e}} = \rho_{\text{crit,0}} \frac{\rho_e}{\rho_{\text{crit,0}}}. \tag{2.1.34}$$

Combining the above equation with the definition of Ω_{gw} we arrive at

$$h^2 \Omega_{\text{gw,0}} = \Omega_{\text{gw}} \left(\frac{a_e}{a_*}\right)^{1-3w} \left(\frac{g_*}{g_0}\right)^{-\frac{1}{3}} \Omega_{\text{rad,0}} h^2, \tag{2.1.35}$$

where I inserted the square of the reduced Hubble constant, in order to eliminate inaccuracies in the measurement of the present day Hubble constant. From here on I will make the further assumption that the universe is radiation dominated ($w = 1/3$) between the end of the simulation and the end of reheating. This must not in general be the case and depends on how the fields participating in reheating couple to the standard model. For simplicity I will assume $w = 1/3$ during that time and I will also use $g_*/g_0 = 100$. Similarly it possible to convert a wave number k_e at the end of inflation to its corresponding frequency that would be measured today (see also [24, 25]):

$$f \approx 2.7 \times 10^{10} \frac{k}{a_e \sqrt{m_{\text{pl}} H_e}} \text{ Hz}. \tag{2.1.36}$$

2.2. Inflation

2.2.1. Motivation

Inflation is a conjectured epoch of the universe that occurred almost directly after the big bang. In this time frame, the energy density of the universe is thought to be dominated by a slowly varying vacuum energy, while the universe underwent a roughly exponential expansion.

This scenario gained a lot of interest after it was shown that various problems of the standard cosmology could be solved by inflation [26]. Three of these problems are as follows:

Flatness problem: The spatial curvature density is observed to take a value very close to zero, which implies that this value must have been even smaller at earlier times. This poses a fine-tuning problem since the value needs to be set precisely to a non-zero value at the big-bang [27–30].

Horizon problem: The cosmic microwave background (CMB) shows an almost perfect isotropic distribution. However, in standard cosmology, it shouldn't have been possible for physical influences to travel far enough in order to smooth out inhomogeneities during the earlier times of the universe [30].

Missing monopoles problem: Many of the proposed grand unified theories (GUT) predict the existence of magnetic monopoles that were created at high temperatures during the early universe. These monopoles should still be observable nowadays but have not been observed so far [31, 32].

Inflation is not a necessity to explain these observations since the flatness and horizon problem could directly be solved by fine-tuning the initial conditions to specific non-trivial values. Inflation provides an alternative explanation to all of the above-stated problems and is, therefore, a popular theory since it does not have the same need for fine-tuning. Inflation addresses the problems in the following ways:

Flatness problem: The spatial curvature naturally decreases during an exponential expansion. While the spatial curvature might have taken a greater value before inflation, it could therefore be brought to a sufficiently small value during inflation.

Horizon problem: In the inflation scenario inhomogeneities could have smoothed out before the inflationary phase took place, thus resulting in an isotropic universe.

Missing monopoles problem: If these monopoles were produced at temperatures before the inflation took place, then they could have been sufficiently diluted during inflation which would naturally explain their sparsity.

For a quantitative investigation into how inflation solves these problems see [33, 34].

2.2.2. Slow-roll inflation

The assumptions of an accelerated expansion usually lead to the so-called slow-roll conditions[2] [36]. For a single homogeneous scalar field, these conditions would read as

$$\frac{1}{2}\dot{\phi}^2 \ll V(\phi) \ \ \text{and} \ \ |\ddot{\phi}| \ll 3H|\dot{\phi}|, \tag{2.2.37}$$

where ϕ is the inflaton field, $V(\phi)$ the corresponding potential energy. The first condition results in the energy density of the universe being dominated by a slowly varying potential energy of the inflaton field which then results in accelerated expansion. The second condition ensures that this expansion is sustained for a sufficiently long amount of time. These conditions are usually realized by having the homogeneous scalar field start from a displacement away from a local minimum and then have it slowly "roll" towards that minimum. This mechanism was studied for a wide range of different models and the resulting cosmological perturbations (the scalar spectral index and the tensor-to-scalar ratio) can be compared to the observational constraint that is provided from the Planck survey [37].

The scalar field will, at some point still away from the minimum, start to violate the slow-roll conditions and thus the universe will not undergo an accelerated phase of expansion anymore. This marks the end of the slow-roll inflation, which leaves the universe in a matterless and super-cooled state.

2.3. Reheating

In order to reheat the universe and to produce the nowadays observed distribution of matter, the inflaton field needs to decay into the necessary forms of matter and radiation. It is hence thought that the phase of inflation is followed by a phase of reheating. After the end of the slow-roll inflation, the inflaton field will start to oscillate around its minimum, which will lead to rapid particle production of the decay particles. In the following, I explain the need for non-perturbative methods and briefly discuss two mechanisms that are known to play a role in reheating models. For general reviews on reheating see [36, 38, 39].

---

[2]Note that it is also possible to have accelerated expansion without having a slow-roll [35].

2.3.1. **Perturbative reheating**

In modern particle physics, perturbative expansions are a popular tool and therefore it was also tried to treat reheating as a perturbative process in which individual inflaton particles decay independently of each other. For this, the decay width Γ_ϕ of the inflaton field would be approximated in the usual manner by calculating the transition amplitude for the inflaton decay to a certain order of the coupling expansion. This approach, however, does not capture the full picture of reheating since especially at the beginning of the reheating phase the perturbative treatment is in general not applicable since the field perturbations can grow to sufficient large extends that a linear treatment of the model is not valid anymore. In the following sections, I will take a look at two mechanisms that are in general of non-perturbative nature and crucial in certain models.

2.3.2. **Reheating mechanisms**

Parametric resonance

Parametric resonance is a mechanism that leads to the exponential growth of certain modes of a scalar field. This mechanism is in general not fully treatable with perturbative methods, which break down for certain configurations. In general parametric resonance can occur when the equations of motion for the respective mode have a form of[3]

$$\ddot{\chi}_k + \omega_k^2(t)\chi_k = 0. \tag{2.3.38}$$

In the case of FRW expansion, the frequency ω can generally be expressed by

$$\omega_k^2 = \left(\frac{k}{a}\right)^2 + m_{\chi,\text{eff}}^2, \tag{2.3.39}$$

where the effective mass $m_{\chi,\text{eff}}$ generically depends on the fields that χ couples to as well as the scale factor and its derivative. A further condition for parametric resonance to occur is that ω needs to violate the adiabatic condition

$$\left|\frac{\dot{\omega}_k(t)}{\omega_k^2(t)}\right| \ll 1. \tag{2.3.40}$$

---

[3]In the case of FRW expansion also a term linear in $\dot{\chi}$ is to be expected. This term can, however, be eliminated by a redefinition of the fields, resulting in the given equation of motion.

After quantizing the field χ in the usual manner, its mode functions will also have to obey the equation in 2.3.38 and from the Floquet theorem we know that for a time-periodic frequency we can write their general solution as

$$u_k(t) = e^{\mu_k t}\mathcal{P}_{k+}(t) + e^{-\mu_k t}\mathcal{P}_{k-}(t), \tag{2.3.41}$$

where the functions $\mathcal{P}_{k\pm}$ are time periodic and the constant μ_k is called the Floquet exponent. If the real part of μ_k is not equal to zero we see that the mode function will grow exponentially.

Tachyonic resonance

If the adiabatic condition in eq. 2.3.40 is fulfilled, then the solution to the individual modes is approximately given by the WKB solution, such that

$$u_k(t) \approx \frac{\alpha_k}{\sqrt{2\omega_k(t)}} \exp\left[-i\int_{t_0}^{t}\omega_k(t')dt'\right] + \frac{\beta_k}{\sqrt{2\omega_k(t)}} \exp\left[i\int_{t_0}^{t}\omega_k(t')dt'\right]. \tag{2.3.42}$$

When $\omega_k^2 < 0$ occurs, then this implies a purely imaginary value for ω_k and since the frequency is not expected to oscillate around zero, this results in one of the two above terms to exponentially grow. Note that since $\omega_k^2 = (k/a)^2 + m_{\chi,\text{eff}}^2 < 0$ this implies an imaginary effective mass (hence the name *tachyonic* reheating). Additionally, we see that this mechanism especially affects the long-wavelength modes since for these it is the easiest to achieve $\omega_k^2 < 0$. This mechanism is also a generic feature of many models, especially those in which symmetry breaking occurs.

2.3.3. Non-linear dynamics and solitons

Models that feature non-linear terms in the equations of motion of the scalar field will generically fragment at some point in time, however, for certain potential, this fragmentation can lead to the formation of interesting formations that can have a lasting impact on the further evolution of the universe. In the context of cosmology, configurations that are stable (or long-lived), localized, and of finite energy are usually referred to as solitons. In general, solitons are distinguished by whether they exist because of topological reasons (topological soliton), or non-topological reasons (non-topological soliton). Common examples for topological solitons are domain walls and cosmic strings that are generically produced due to symmetry breaking. This work will however focus on the non-topological soliton called oscillon, which will be defined in detail in the next chapter.

3. Oscillons

I will give a short overview of oscillons and similar structures and afterward discuss their profile and aspects of how they can produce GWs. A recent review on the analytical, as well as numerical aspects of oscillons is given in [10].

3.1. Overview

Oscillons are quasi-stable localized oscillations of a real scalar field that generically appear in models with a potential that is 'shallower' than quadratic around its minimum. During their life, they emit scalar waves (waves in their respective field) that lead to an energy loss which eventually destabilizes the oscillon. Oscillons are of great interest in the context of cosmological studies as they generically appear in models of scalar field driven inflation during the reheating phase when the inflaton oscillates around the minimum of its potential [5, 6, 10–13]. The produced oscillons can inhibit a large fraction of the energy density and can therefore be crucial for the subsequent evolution of the universe. It has been shown that especially the formation process of oscillons can result in a distinctive GW spectrum that could be detectable in the future [14, 15, 17, 40, 41]. With precision measurements of the GW background, it will therefore be possible to further restrict the range of possible inflation and reheating models. For this reason, it is important to further study the production, life, and decay of oscillons.

Structures similar to oscillons also occur in models that feature a conserved charge, which is then associated with the stability of the oscillons. If this charge is the result of a global $U(1)$ symmetry, such as for a generic complex scalar field, then the resulting structures are called Q-balls [42]. While oscillons are formed due to self-interactions of the scalar field, gravitation also naturally leads to fragmentation into spherical lumps similar to oscillons. In this case a distinction is made and the structures are instead called oscillatons [10]. It was shown that oscillons could in the standard model if the Higgs mass were two times that of the $W^{\pm}$ bosons [12, 43,

44]. Since this is not the case oscillons don't seem to be a feature of the standard model, but they are shown to naturally occur in a variety of supersymmetric models [11, 45] as well as Lorentz symmetry violating models [46]. Furthermore, oscillons might play a role in primordial black hole formation [8, 47], dark matter [8, 48] and boson stars [49]. Oscillons are also shown to emerge in general Bose-Einstein condensates [50].

3.2. Profile

Oscillons can be studied by using analytical method as well as simulations. The basic classical field equation for a real scalar field ϕ with potential $U(\phi)$ on flat Minkowski background $g_{\mu\nu} = (-1, 1, \ldots, 1)$ is given by

$$-\frac{\partial^2 \phi}{\partial t^2} + \Delta \phi = U'(\phi), \tag{3.2.1}$$

where the prime denotes differentiation with respect to the field ϕ. We are interested in the dynamics of the field close to its vacuum state, therefore it is useful to write the potential in an expansion around its minimum

$$U(\phi) = \frac{1}{2} m^2 \phi^2 + \sum_{k=2}^{\infty} \frac{1}{k+1} g_k \phi^{k+1}. \tag{3.2.2}$$

In general, we can expand the field in terms of a parameter ϵ, such that

$$\phi = \sum_{k=1}^{\infty} \epsilon^k \phi_k. \tag{3.2.3}$$

This is known as the small-amplitude expansion. In the following, I will shortly summarize the procedure by which the solutions to the individual components ϕ_k are obtained. The complete derivation is however given in [10]. Firstly, it is advantageous to work in spherical coordinates and to introduce rescaled time and space coordinates such that

$$\rho = \epsilon r, \quad \tau = \omega(\epsilon) t, \tag{3.2.4}$$

where r is the distance to the center of the oscillon and ω is a characteristic frequency of the oscillon that is dependent on ϵ. Rescaling the distance in this manner is sensible since the oscillons size is also expected to increase with increasing amplitude.

From here on I will additionally use units such that $m = 1$. Expanding ω thus gives

$$\omega(\epsilon) = 1 + \sum_{k=1}^{\infty} \epsilon^k \omega_k, \tag{3.2.5}$$

where it was used that $w(\epsilon) \xrightarrow{\epsilon \to 0} m = 1$. Plugging the relations in 3.2.4, 3.2.5 into eq. 3.2.1 results in

$$-\omega^2 \frac{\partial^2 \phi}{\partial \tau^2} + \epsilon^2 \Delta_\rho \phi = \phi + \sum_{k=2}^{\infty} g_k \phi^k, \tag{3.2.6}$$

where Δ_ρ is the Laplacian with respect to the new radial coordinate ρ. Using the field expansion given in 3.2.3, the equations can be sorted by powers of ϵ and then iteratively solved to obtain the oscillon profile. At each iteration three assumptions are made about the ϕ_k: They will fall off to zero at infinity, they are bounded and they are periodic in time. These assumptions allow discarding solutions that do not actually represent oscillons. For a general potential, the solutions to the first four ϕ_k are given by

$$\phi_1 = p_1 \cos \tau, \tag{3.2.7a}$$

$$\phi_2 = \frac{g_2}{6} p_1^2 \left[\cos(2\tau) - 3 \right], \tag{3.2.7b}$$

$$\phi_3 = p_3 \cos \tau + \frac{1}{72} \left(4g_2^2 - 3\lambda \right) p_1^3 \cos(3\tau), \tag{3.2.7c}$$

$$\phi_4 = -g_2 p_1^2 - g_2 p_1 p_3 + \frac{1}{6} g_2 \lambda p_1^4 - g_2 \left(\frac{dp_1}{d\rho} \right)^2 + \frac{31}{72} g_2^3 p_1^4 - \frac{3}{8} g_4 p_1^4 \tag{3.2.7d}$$

$$- \frac{g_2 p_1^4}{72} \left[\frac{8}{p_1^4} \left(\frac{dp_1}{d\rho} \right)^2 - 12 \frac{g_4}{g_1} + 16 g_2^2 - 24 \frac{p_3}{p_1^3} - 23\lambda - \frac{8}{p_1^2} \right] \cos(2\tau)$$

$$+ \frac{1}{360} p_1^4 (3g_4 - 5g_2\lambda + 5g_2^3) \cos(4\tau),$$

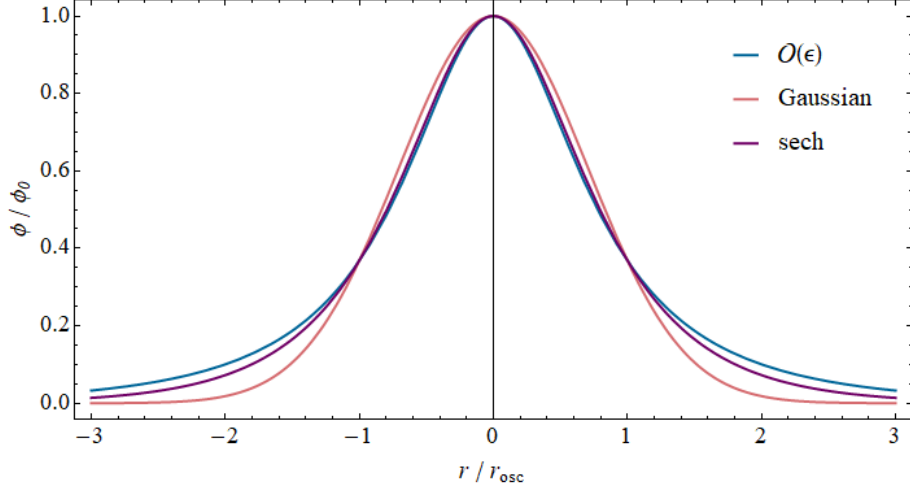where the constant λ and the functions p_1 and p_3 were introduced. These are given

Figure 3.1.: The figure display the oscillon profile to first order in ϵ, as well as a Gaussian function and a hyperbolic secant function that are all normalized to have the value of $1/e$ at $r = r_{\mathrm{osc}}$. The potential $V(\phi) = \phi^2(\phi - 1)/8$ was used to construct the oscillon profile.

by

$$\lambda = \frac{5}{6}g_2^2 - \frac{3}{4}g_3, \tag{3.2.8a}$$

$$\Delta_\rho p_1 = \lambda p_1^3 - p_1, \tag{3.2.8b}$$

$$p_3 = \frac{1}{\lambda^2 \sqrt{\lambda}} \left[\sigma Z - \frac{1}{54} \lambda^{3/2} g_2^2 p_1 \left(32 + 19 \lambda p_1^2 \right) \right] \tag{3.2.8c}$$

$$\Delta_\rho Z = Z - 3\lambda p_1^2 Z + \lambda^{5/2} p_1^5, \tag{3.2.8d}$$

$$\sigma = \frac{1}{24}\lambda^2 - \frac{1}{6}\lambda g_2^2 + \frac{5}{8}g_5 - \frac{7}{4}g_2 g_4 + \frac{35}{27}g_2^4. \tag{3.2.8e}$$

As can be seen, the expansion becomes increasingly complicated for higher correction terms. Note that in general, the profile will have time dependence that consists of a sum with terms proportional to $\cos(n\tau)$. It can be shown that modes with $n > 1$ cause the oscillon to emit radiation and thus eventually lead to its decay. The above expressions somewhat simplify if a symmetric potential is used (see [10] for corrections up to ϕ_6 for a symmetric potential). While this expansion is valid for an arbitrary potential, for certain potentials it is more useful to use a different expansion that is specific to the potential. Figure 3.1 displays the profile as it is obtained from the small-amplitude expansion at linear order. For comparison, a hyperbolic secant and a Gaussian is also shown. While the hyperbolic secant seems to approximate the
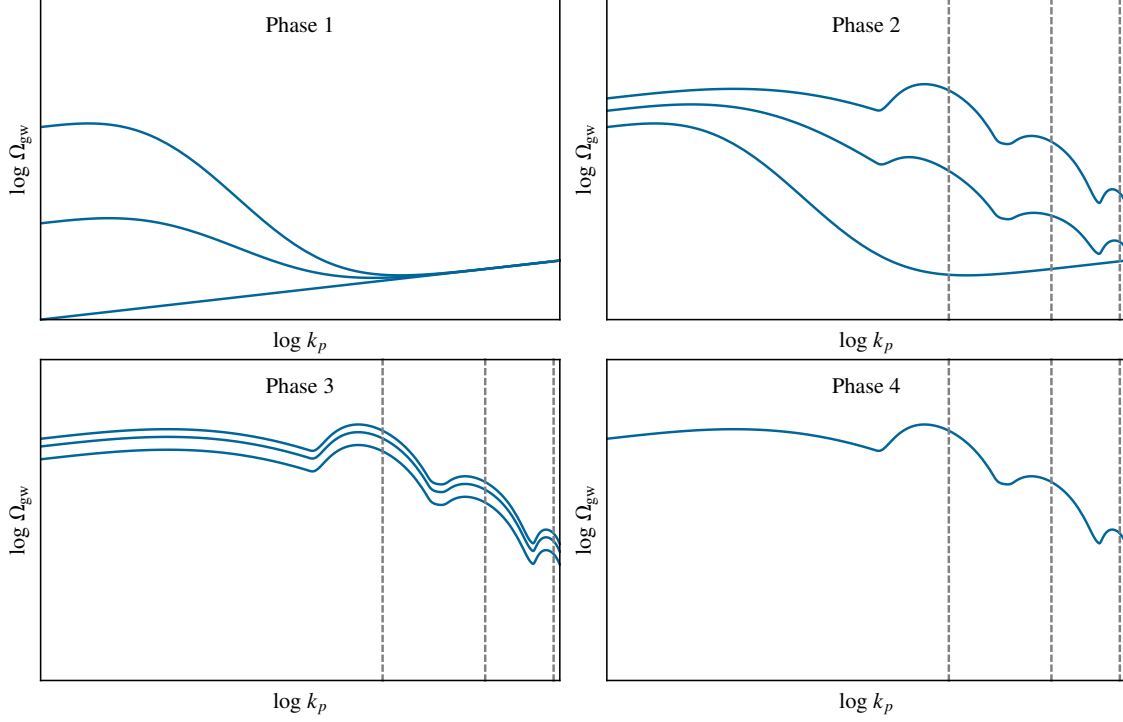
Figure 3.2.: The figure shows four distinct phases for the spectrum of GWs. See the text for more information.

profile better, a Gaussian is often used to ease (or enable) analytical calculations.

In this way, it is also possible to calculate the classical decay rate [51] as well as the decay rate for the quantized model [52]. It can additionally be shown that one of the conditions for the existence of oscillons is that the potential needs to be "shallower" than quadratic at the minimum (see e.g. [10, 53]).

3.3. Gravitational waves

If oscillons were perfectly spherical objects, then they would in general not radiate GWs according to Birkhoff's theorem. However, in reality, the profile will not be exactly spherical and the asymmetries will result in the production of GWs [15, 17]. Further, events such as oscillon collisions and the decay of oscillons could also produce GWs.

The gravitational spectrum that is produced during reheating in combination with oscillons can usually be separated into four distinct phases. These are illustrated in fig. 3.2 and are as follows:

3. Oscillons

Phase 1: Power in low momentum modes of the scalar field grows exponentially due to a reheating mechanism (parametric or tachyonic resonance) and source GWs. The perturbations are however still small compared to the background field and are thus treatable at linear order.

Phase 2: Perturbations in the scalar field grow large enough that the linear order does not capture the evolution accurately anymore. Instead, the non-linear interactions typically lead to an up-scattering (sometimes also referred to as re-scattering) that transfers energy to higher momentum modes. Additionally, oscillons start to form during this process and impact the GW spectrum by resulting in roughly equally spaced peaks at physical momenta that correspond to the typical oscillation frequency $\sim m_\phi$ of the oscillons and their higher harmonics (gray dashed lines in the figure).

Phase 3: Up-scattering stops and oscillons start to stabilize by being driven to spherical configurations. During this process, only a small amount of power is added to the GW spectrum.

Phase 4: Oscillons are stable and almost perfectly spherical. The emission of GW is therefore highly suppressed and the spectrum effectively only changes by being redshifted due to the expansion of space.

Note that in general the relative height of the GW spectrum caused by the reheating mechanism and the oscillons is model dependent, meaning that the oscillons do not necessarily have to give rise to any pronounced features in the GW spectrum (see [18]).

4. Numerical methods

In order to understand the dynamics of oscillons and GWs during reheating better, it is necessary to employ numerical simulations. While there already exist programs that are publicly available for the simulation of reheating, such as PyCOOL [54], HLATTICE [55], GABE [56], they usually employ a second-order accurate approximation to the Laplacian. However, we will later see that this approximation can be insufficient for the simulation of GWs. While there also exists code that utilizes the pseudospectral method, such as PSpectRe [57], these simulations typically take longer run times due to the need of calculating the Fourier transform at every time step. Moreover, due to advancements in technology, it has become more viable in the last decade to use graphics processing units (GPUs) for lattice simulations. In contrast to regular central processing units (CPUs), GPUs can handle thousands of threads in parallel and have faster memory access to the extent that a single GPU can often outperform multiple CPU nodes on a cluster. For this reason, code was developed on the basis of LatticeEasy [58] using the newest compute unified device architecture (CUDA) toolkit, which is being developed by Nvidia [19] .

In this chapter, I will first discuss how the dynamics of a scalar field are handled in LatticeEasy and afterward, I will explain how the program was modified to also incorporate the dynamics of GWs. More details on the used stencil and CUDA implementation can be found in appendix A.

4.1. Standard LatticeEasy

LatticeEasy is designed to simulate the classical dynamics of multiple scalar fields on a square lattice with periodic boundary conditions. This is achieved by discretizing the equation of motion of the scalar field given in 2.1.8. Additionally, rescalings are used to eliminate the friction term from the equation of motion (for details see [58]). The field values are initialized in momentum space according to quantum

fluctuations that are characterized by

$$|\phi_k| = \frac{1}{\sqrt{2\omega_k}}, \tag{4.1.1}$$

where f_k is the kth mode of the fields Fourier transform and

$$\omega_k^2 = k^2 + m_{\text{eff}}^2, \quad \text{with} \quad m_{\text{eff}}^2 = \frac{\partial^2 V}{\partial \phi^2}. \tag{4.1.2}$$

The scale factor is evolved by utilizing the first equation in 2.1.6, where the mean energy density within the simulation volume $\mathcal{V}$ is used:

$$H^2 = \frac{1}{3m_{\text{pl}}^2} \langle \rho \rangle_{\mathcal{V}} = \frac{1}{3m_{\text{pl}}^2} \left\langle \frac{1}{2}\dot{\phi}^2 + \frac{1}{2a^2}(\nabla\phi)^2 + V(\phi) \right\rangle_{\mathcal{V}}. \tag{4.1.3}$$

The Laplacian in the equation of motion of the scalar field is calculated using the standard 7-point nearest neighbor stencil. This does usually not prove to be enough accuracy for simulations that aim to investigate the production of GWs. LatticeEasy uses a staggered leapfrog scheme, which means, that the values of the field and the field derivative are stored at different times, which increases the accuracy of the code. Using other methods such as Runge-Kutta would result in even better accuracy with a cost on execution time and increased memory demand.

4.2. Lattice derivatives

It is necessary to calculate derivatives on the lattice at three separate places: The Laplacian in the equation of motion (eq. 2.1.8), the gradient for the evolution of the scale factor (eq. 4.1.3), and the directional derivatives for the EMT (eq. 2.1.3). LatticeEasy uses in the first two cases derivatives that are based on the nearest neighbor, which are therefore second-order accurate. However, using only the nearest neighbors has some drawbacks, such as the truncation error of the Laplacian being dependent on direction, thus introducing anisotropic artifacts. As was discussed in [59, 60] a more accurate stencil can be constructed by considering all 26 neighbors, which results in a stencil that is still second-order accurate, but 4th order isotropic. In 4.1 the values of stencil coefficients for three of these isotropic stencils are given. In the following, I will refer to the isotropic C stencil as isoC. Additionally, I have derived a stencil that is 4th order accurate and 6th order isotropic (see section A.2), which I will refer to as isoD. Table 4.1 shows the coefficients for the first-order one-

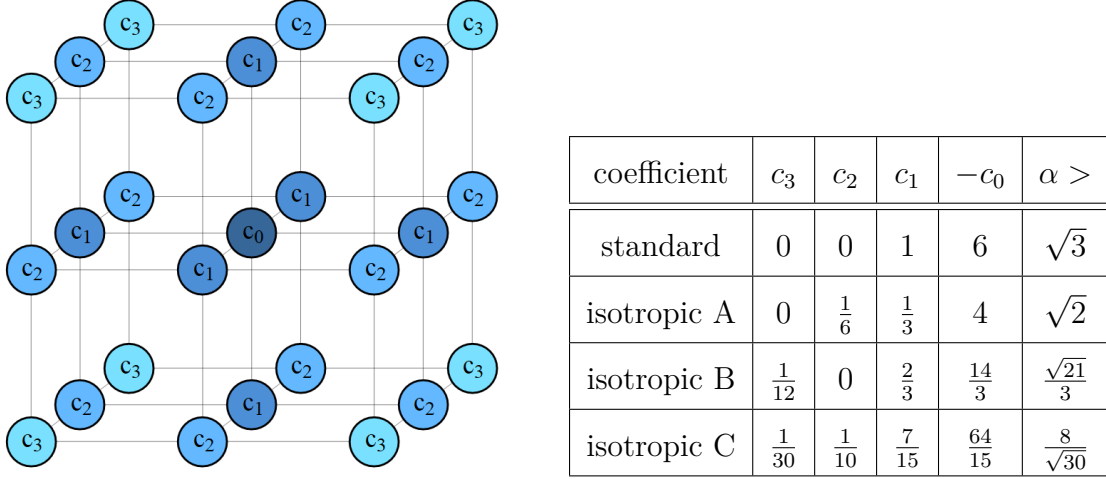| coefficient	c_3	c_2	c_1	$-c_0$	$\alpha >$
standard	0	0	1	6	$\sqrt{3}$
isotropic A	0	$\frac{1}{6}$	$\frac{1}{3}$	4	$\sqrt{2}$
isotropic B	$\frac{1}{12}$	0	$\frac{2}{3}$	$\frac{14}{3}$	$\frac{\sqrt{21}}{3}$
isotropic C	$\frac{1}{30}$	$\frac{1}{10}$	$\frac{7}{15}$	$\frac{64}{15}$	$\frac{8}{\sqrt{30}}$

Figure 4.1.: A general 27 point stencil for the calculation of the Laplacian. Due to the symmetry of the Laplacian. The figure on the left side shows the spatial position of each coefficient, while the table on the right shows the coefficient values. The value in the last column is an approximation to the minimum value for $\alpha = dx/dt$ such that the simulation can run stable (see section A.2.2).

directional derivative up to order $\mathcal{O}(dx^8)$. The program is designed such that stencils are easily replaced by higher (or lower) order stencils. In sec. 5.1 I will investigate what impact the different stencils have on the results of the simulation.

4.3. TT-projector

Since GWs are represented by the TT part of the tensor perturbations, it is necessary to define a projector that allows extracting this part from a given tensor. In the continuum limit, this projector is given in Fourier space by

$$\Lambda_{ij,lm}(\hat{k}) = P_{il}(\hat{k})P_{jm}(\hat{k}) - \frac{1}{2}P_{ij}(\hat{k})P_{lm}(\hat{k}), \quad P_{ij}(\hat{k}) = \delta_{ij} - \hat{k}_i\hat{k}_j, \quad \hat{k} = \frac{k}{|k|}, \quad (4.3.4)$$

such that for a given tensor $\Pi_{ij}(k)$ we have

$$\Pi_{ij}^{\mathrm{TT}}(k) = \Lambda_{ij,lm}(\hat{k})\Pi_{lm}(k). \quad (4.3.5)$$

Note that this projector is linear in Fourier space. While this works in the continuum, this projector will give wrong results due to a leak of scalar modes on a lattice, as

4. Numerical methods

$\mathcal{O}(dx^n)$	Coefficients at the relative positions								
	-4	-3	-2	-1	0	1	2	3	4
$\mathcal{O}(dx^2)$				$-\frac{1}{2}$	0	$\frac{1}{2}$			
$\mathcal{O}(dx^4)$			$\frac{1}{12}$	$-\frac{2}{3}$	0	$\frac{2}{3}$	$-\frac{1}{12}$		
$\mathcal{O}(dx^6)$		$-\frac{1}{60}$	$\frac{3}{20}$	$-\frac{3}{4}$	0	$\frac{3}{4}$	$-\frac{3}{20}$	$\frac{1}{60}$	
$\mathcal{O}(dx^8)$	$\frac{1}{280}$	$-\frac{4}{105}$	$\frac{1}{5}$	$-\frac{4}{5}$	0	$\frac{4}{5}$	$-\frac{1}{5}$	$\frac{4}{105}$	$-\frac{1}{280}$

Table 4.1.: The table shows the coefficients for the one directional first order deriva-
tive at the positions relative to the point of interest (i.e. -1 corresponds
to a distance of $-dx$ from the point at which the derivative is to be cal-
culated). The truncation error for each stencil is shown in the left most
column. Taken from [61].

was shown in [62]. The authors therein presented a modified projector that takes
the used lattice derivative into account by constructing a lattice-specific momentum.
The first-order derivative in direction $\mathbf{i}$ on the lattice can be written as

$$\partial_{\mathbf{i}}\phi(\mathbf{n}) = \sum_m D_{\mathbf{i}}(\mathbf{n} - \mathbf{m})\phi(\mathbf{m}), \tag{4.3.6}$$

where bold quantities such as $\mathbf{n}$ denote the position on the lattice. In the following
I will only consider the neutral finite difference stencils that are given in table 4.1,
such that

$$D_i(\mathbf{n}) = \frac{1}{dx}\sum_l c_l \left(\delta_{\mathbf{n},-l\mathbf{i}} - \delta_{\mathbf{n},+l\mathbf{i}}\right). \tag{4.3.7}$$

The effective momentum is then constructed by considering the Fourier transform
of the field that results from acting the derivative on each lattice point, such that

$$\mathcal{F}\left[D_i f\right](\tilde{\mathbf{n}}) = -i k_{\text{eff}}(\tilde{\mathbf{n}})\mathcal{F}\left[f\right](\tilde{\mathbf{n}}), \tag{4.3.8}$$

where $\mathcal{F}[\dots]$ explicitly denotes the discrete Fourier transform on the lattice and $\tilde{\mathbf{n}}$
labels the reciprocal lattice, i.e. $\tilde{n}_i = -N/2+1,\dots,N/2$. Using the above definition
results in

$$k_{\text{eff},i}(\tilde{\mathbf{n}}) = i\sum_{\mathbf{n}} e^{\frac{2\pi i}{N}\tilde{\mathbf{n}}\cdot\mathbf{n}} D_i(\mathbf{n}). \tag{4.3.9}$$

We, therefore, obtain for the directional derivative

$$k_{\mathrm{eff},i}(\tilde{\mathbf{n}}) = \frac{i}{dx} \sum_l c_l \left(e^{-l\frac{2\pi i}{N}\tilde{\mathbf{n}}\cdot\mathbf{i}} - e^{l\frac{2\pi i}{N}\tilde{\mathbf{n}}\cdot\mathbf{i}} \right) = \frac{2}{dx} \sum_l c_l \sin\left(l\frac{2\pi}{N}\tilde{n}_i \right). \qquad (4.3.10)$$

However, it should be noted that using this modified lattice projector is not completely consistent. This is because the utilized Laplacian stencil is not the same as combining the directional derivatives in a way to calculate the Laplacian. However, we will later see in section 5.7 that the modified projector still provides more accurate results than the continuum projector.

4.4. Gravitational wave simulation

As was discussed in 2.1.3, the equation of motion for the tensor perturbations are

$$\ddot{h}_{ij} + 3H\dot{h}_{ij} - \frac{1}{a^2}\nabla^2 h_{ij} = \frac{2}{m_{\mathrm{Pl}}^2 a^2} T_{ij}^{\mathrm{TT}}, \qquad (4.4.11)$$

with $T_{\mu\nu}^{\mathrm{TT}} = [\partial_\mu\phi\partial^\nu\phi + g_{\mu\nu}(\mathcal{L} - \langle p\rangle)]^{\mathrm{TT}}$ being the TT part of the EMT. However, it would be computationally costly to calculate the TT projection of the EMT at every time step, as it would be necessary to first Fourier transform all components of T_{ij}, then projecting it to TT space and then back transforming it to configuration space. Instead, as was done in [63], I am evolving the tensor perturbations using an effective EMT and then only TT project the tensor h_{ij} at times that an output needs to be generated. More clearly, the term in $T_{\mu\nu}$ that is proportional to $g_{\mu\nu}$ can be decomposed into one term proportional to δ_{ij} and another proportional to h_{ij}. The one with δ_{ij} will not contribute to the TT part, as it is a pure trace. Further, the other term containing h_{ij} is of second order in h and can therefore be neglected. We can therefore define an effective EMT that only contain the parts that actually source GWs, which is given by $\Pi_{\mu\nu}^{\mathrm{eff}} = \partial_\mu\phi\partial^\mu\phi$. Note that this effective EMT will however source not only the GWs, which means that TT projecting will still be necessary. Using the effective EMT the program will evolve the following equation of motion

$$\ddot{u}_{ij} + 3H\dot{u}_{ij} - \frac{1}{a^2}\nabla^2 u_{ij} = \frac{2}{m_{\mathrm{Pl}}^2 a^2} T_{ij}^{\mathrm{eff}}. \qquad (4.4.12)$$

Whenever an output needs to be generated, we can obtain the actual tensor per-

turbation h_{ij} by first Fourier transforming u_{ij} and then applying the TT projector that was discussed in the previous section. We can see that this procedure will give the same result as using T_{ij}^{TT} as the source, since applying the TT projector to the above equation will recover the original equations of motion 4.4.11. We, therefore, exploited the linear nature of the TT projector to commute it with the evolution of the tensor perturbation. In total it is therefore only necessary to Fourier transform and TT project at times that output is generated, significantly improving the execution time of the simulations.

5. Results

After presenting and discussing tests that were done to validate the written code, I will investigate the GWs that are produced in a hilltop model during reheating in the case that the inflaton is coupled to an additional scalar field.

5.1. Code validation

The code validation is done for the evolution of the scalar field and the generated gravitational fields separately: In the following section, I will first present the results of the scalar field evolution and compare it to a previously made publication. Afterward, I will use a different model in which the gravitational fields were studied in detail.

5.1.1. Scalar field evolution

To validate the scalar field evolution, I will evolve the model given in [1] and compare the resulting spectrum of the scalar field. Specifically, the model is that of a scalar field in a sextic potential:

$$V(\phi) = \frac{m^2}{2}\phi^2 - \frac{\lambda}{4}\phi^4 + \frac{g^2}{6m^2}\phi^6. \tag{5.1.1}$$

This potential can be understood as an approximation to the ground state of the inflaton and thus only models the reheating phase. The run parameters are summarized in table 5.1. These are chosen such that the field undergoes parametric resonance right in the beginning and subsequently, the created field perturbations collapse to form oscillons, as is shown in fig. 5.1. All four panels in fig. 5.2 show the field fluctuation for different values of the scale factor. The top left panel are the reference spectra taken from [1]. The other three panels show the resulting spectra as produced by my code with the isoD, isoC, and sta (standard nearest neighbor) stencils. The reference spectra feature a large peak at $k_p = k/a \leq 0.7m$ and a small

m/m_pl	λ	g	H_i/m_pl
5×10^{-6}	2.8125×10^{-6}	$\lambda/\sqrt{0.1}$	1.8×10^{-9}

ϕ_i/m_pl	$\dot{\phi}_i/m_\mathrm{pl}^2$	N	$L\,m_\phi$	$dt\,m_\phi$
7.3×10^{-4}	4.2×10^{-12}	256	200	0.05

Table 5.1.: Parameter used for the simulation of the model with potential shown in eq. 5.1.1. For more information see the original work in [1].

peak that is located at $k_p \approx 1.1m$ for $a = 1.6$ and is subsequently redshifted to lower values. Both of these features seem to be accurately captured by all three stencils (note that it is not clear whether the spectra of the reference is given at exactly the mentioned scale factors, or if the scale factors were rounded, giving some freedom in the actual position of the second peak). However, the isoC and sta stencil both result in the spectrum growing in the region of $k_p \geq 1.0m$, which is a feature that should not be present in the spectra according to the reference. This growth does not occur due to the simulation being unstable with regards to the respective stencil, but instead originates from inaccuracies caused by using a first order approximation to the Laplacian. However, this growth is not present in the simulation that uses the isoD stencil, which seems to capture all features that are present in the reference spectra correctly.

In general, it is of course not possible to conclude from a single model being simulation accurately whether the code will give accurate results for other models as well. It is however possible to conclude that the individual components of the code, i.e. the initialization, evolution and output of field data seem to function properly with regards to this model.

5.1.2. Gravitational wave evolution

In order to validate the evolution of GWs, I will compare the resulting fractional energy spectrum to the one obtained in a recent convergence study [18]. The authors of this reference noted that in a previous work a peak in the GW spectrum was observed [17], which however did not pass a convergence test. The potential for this
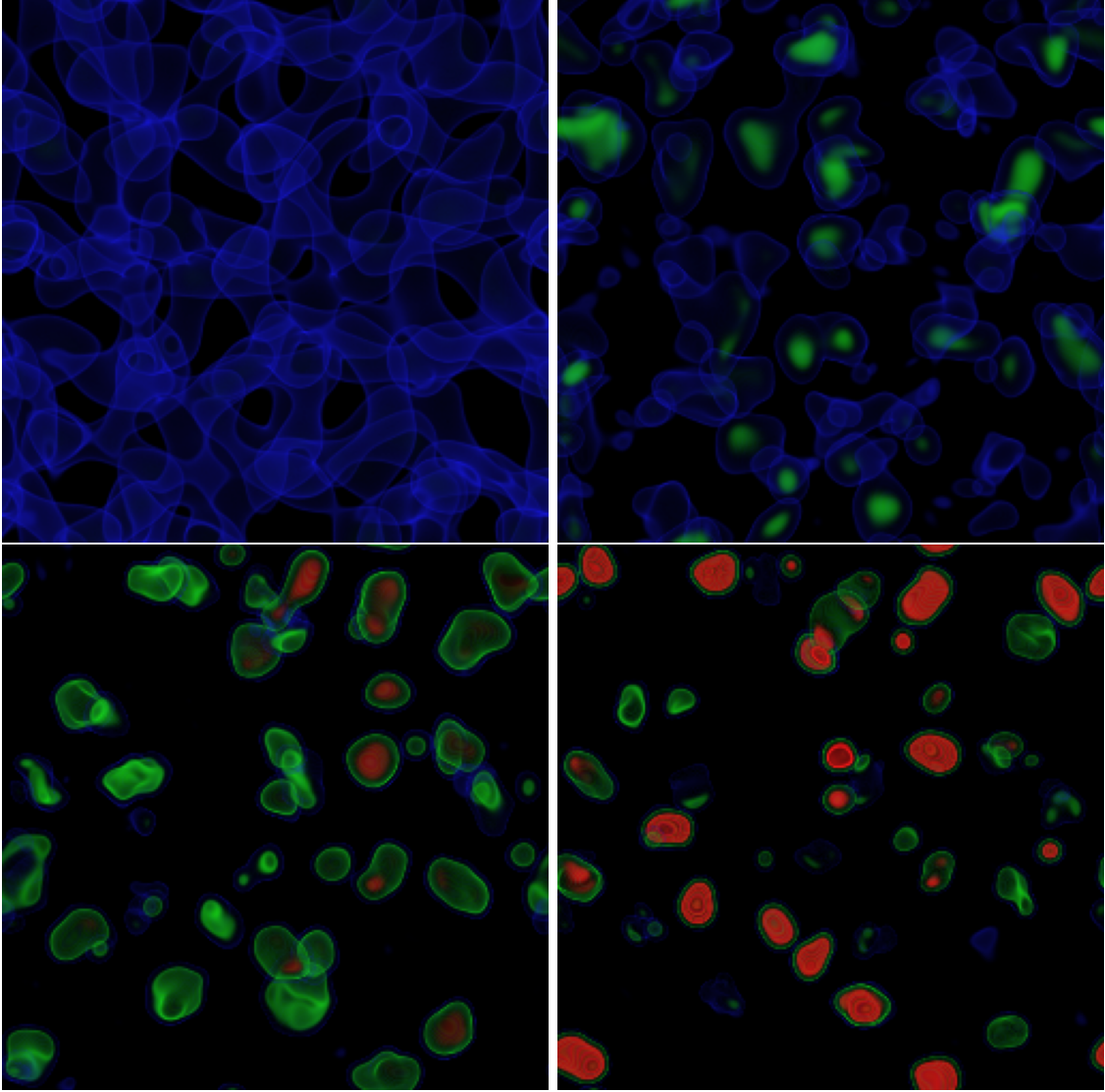
Figure 5.1.: Volume render of overdensities in the sextic model at $a = 1.9$, 2.3, 3.7 and 4.7 (top left to bottom right). Simulated on a lattice with $N = 256$. Gaussian distributions were used as the transfer functions, which are centered at overdensities $\rho / \langle \rho \rangle_\mathcal{V} = 2.5$ (blue), 13.0 (green) and 65.0 (red). Their standard deviation was set to $\sigma = 0.4$ (blue), 3.0 (green) and 12.0 (red).
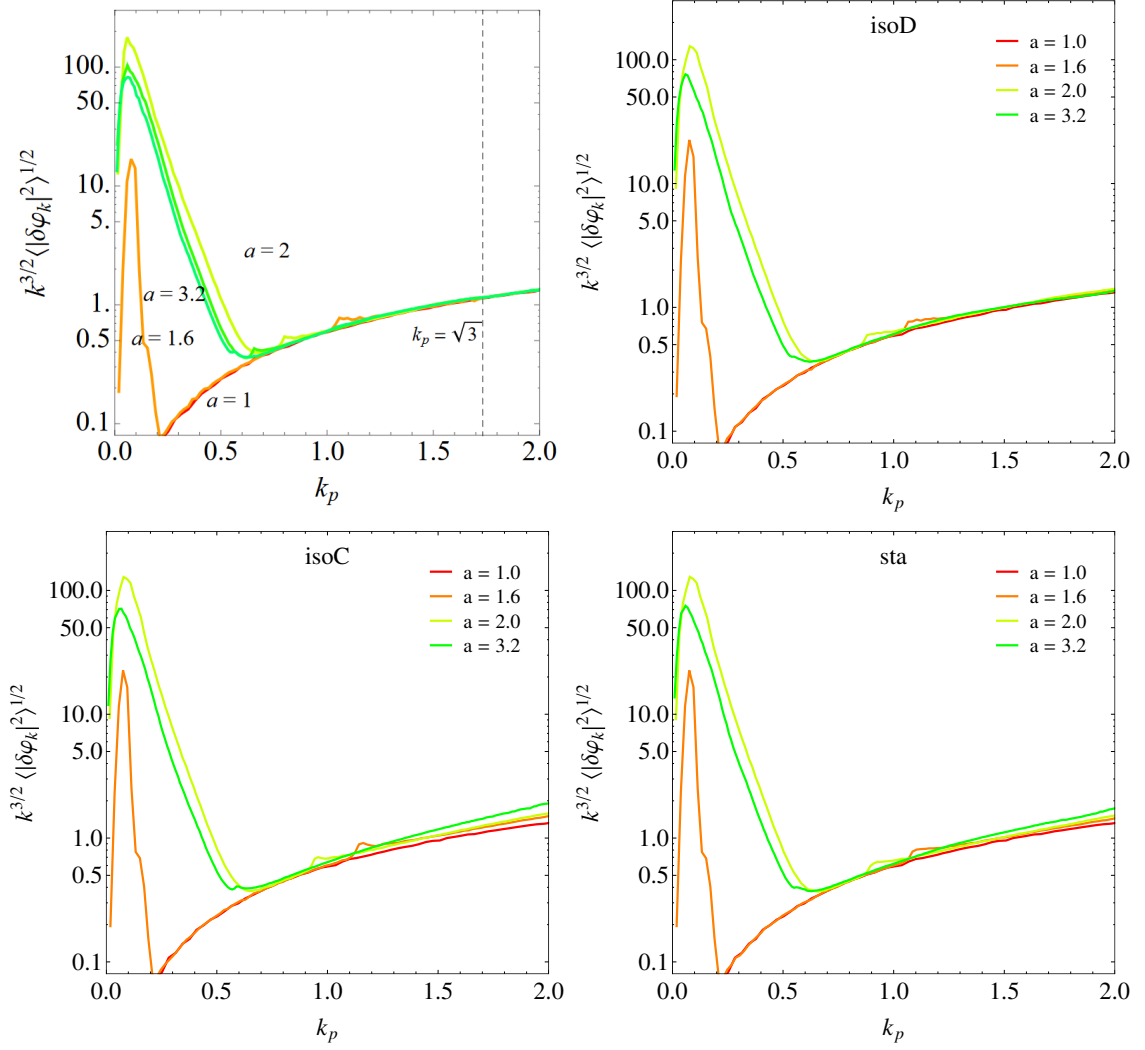
5. Results

Figure 5.2.: The top left panel shows the reference spectra for the scalar field model as described in the text. The other three panel display the spectra as it results by using either the isoD, isoC or sta stencil in the developed code.

model is

$$V(\phi) = V_0 \left(1 - \frac{\phi^6}{v^6} \right)^2 \tag{5.1.2}$$

and all simulation parameters are shown in table 5.3. These are here chosen such that field modes with $k \leq 500 \, m_{\mathrm{pl}}/Hi$ experience tachyonic growth. The authors of the reference paper used the pseudospectral method to obtain the spatial derivatives and a fourth-order Runge-Kutta scheme to evolve the fields in time. They ran the same

v/m_pl	V_0/m_pl^4	m_ϕ/m_pl	H_i/m_ϕ	$L\,m_\phi$	ϕ_i/m_pl	$\dot{\phi}_i/m_\text{pl}^2$	$dt\,m_\phi$
10^{-2}	10^{-19}	2.68×10^{-7}	6.78×10^{-4}	19.05	$0.877v$	$3.73 \times 10^{-6}v^2$	0.02

Table 5.2.: Parameter used for the simulation of the model with potential shown in eq. 5.1.2. For more information see the original work in [18].

simulation for three cases of lattice points per side: $N = 64$, $N = 128$ and $N = 256$. The output times were chosen such $a(t)dx = a(t)L/N \approx 1/m_\phi$, respectively. They found that around this point, the simulations could not be trusted anymore, since the discretization of the system does not accurately capture its dynamics. This is due to the oscillons not being sufficiently resolved anymore since their typical physical size is given by $\sim \mathcal{O}(1)m_\phi^{-1}$. In fig. 5.3 a volume render of the fragmentation process for this model is shown. Two oscillons are there visible, which both seem fully formed at $a \approx 6.0$ and do not show any significant asymmetries. In the following, I will first directly compare the GW spectrum to the one given in the reference and afterward, I will further investigate how the Laplacian stencil, the directional derivatives, and the TT projection affect this spectrum.

Overall

The left side of fig. 5.4 shows the spectra as they are presented in [18], while the right side shows the spectra as it is obtained from the here performed simulations, where the isoD stencil was used together with a 4th order accurate stencil for the directional derivatives. Note that all simulations feature a peak at the high end of the spectrum, which is not a physical peak[1], but is caused due to the finite resolution. In general, it is always expected to find nonphysical noise towards the Nyquist frequencies since they are not well resolved. Also, the here performed simulations seem to generally have too little power in the lowest frequency. In general, it is, again, not expected that this frequency should have accurate results since it is calculated from only 6 points on the reciprocal lattice. However, this does not explain why the resulting value is always too low. The cause of this is not exactly known, but most likely due to precision loss. The spectra show otherwise good agreement with the reference, except for $a = 13.45$, where even the simulation with $N = 256$ resulted in the formation of a plateau at $k_p/H_i \approx 10^3$, indicating that the discretization did not capture the dynamics fully at this point anymore.

---

[1]If it were physical, it should converge to a certain position for growing values of N, but instead it remains at the upper end of the spectrum.
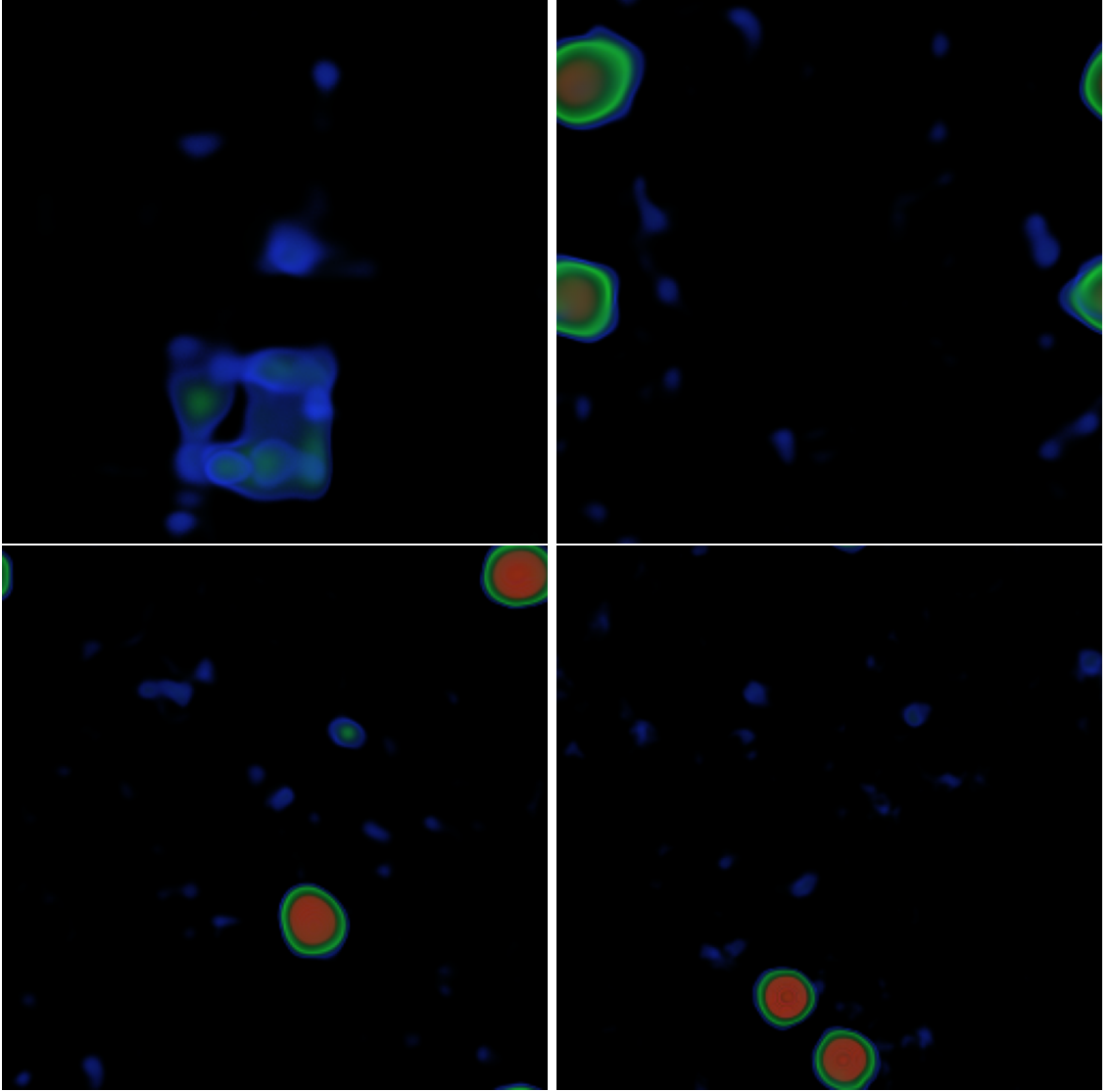
Figure 5.3.: Volume render of overdensities in the hilltop model at $a = 1.5,\ 3.5,$
6.0 and 9.0 (top left to bottom right). Simulated on a lattice with
$N = 256$. Gaussian distributions were used as the transfer functions,
which are centered at overdensities $\rho/\langle\rho\rangle_{\mathcal{V}} = 7.0$ (blue), 15.0 (green)
and 80.0 (red). Their standard deviation was set to $\sigma = 1.0$ (blue), 4.0
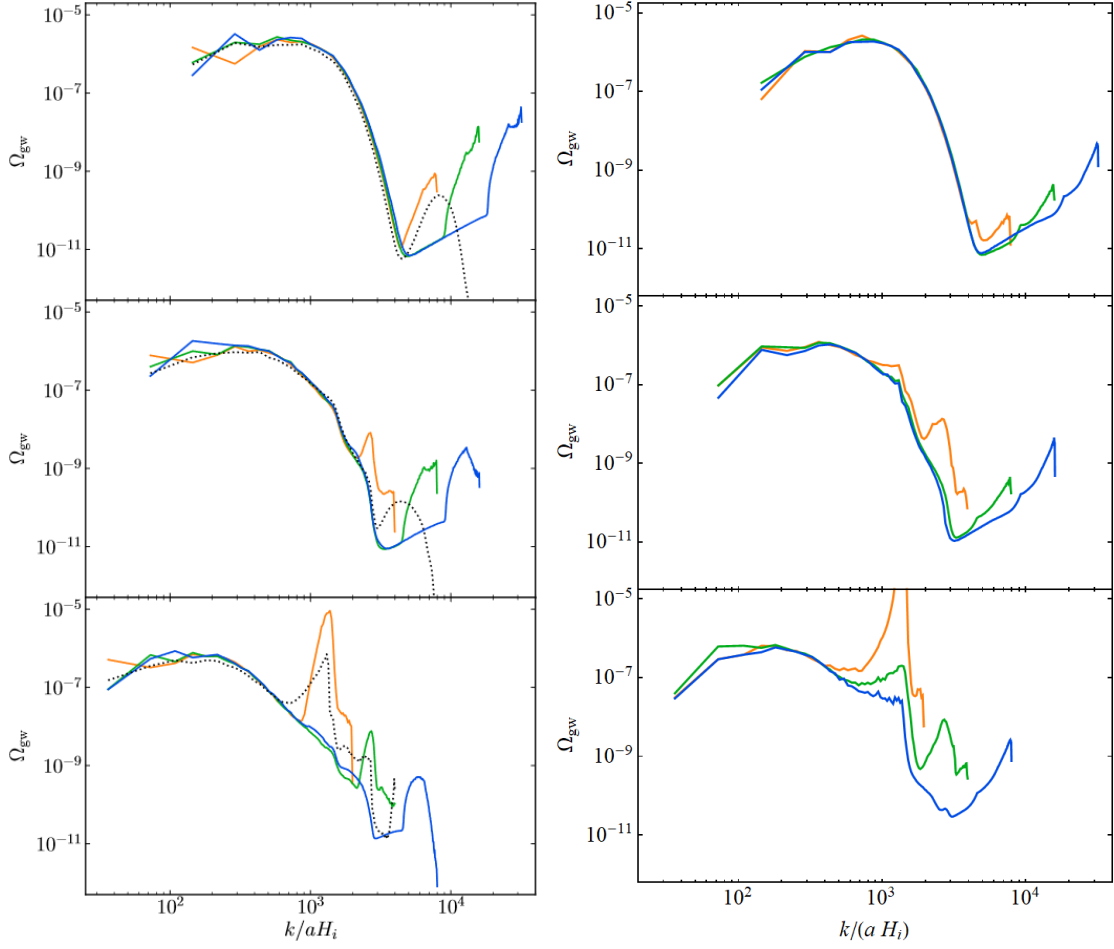(green) and 20.0 (red).

Figure 5.4.: Left: The reference spectra of GWs for the model described in the text. Taken from [18]. Right: Spectra of GWs obtained from the performed simulations, where the isoD stencil was used together with a 4th order stencil for directional derivatives and the custom TT projector. The top panels are taken at $a = 3.35$, the middle panels at $a = 6.7$ and the bottom panels at $a = 13.45$. Each panel shows a simulation made with $N = 64$ (orange curve), $N = 128$ (green curve) and $N = 256$ (blue curve). The reference additionally features a simulation made with nearest neighbor derivatives and $N = 128$ that is shown as the gray dashed line.

5. Results

Laplace stencil

It is useful to compare the GW spectrum produced by the isoD stencil to the isoC stencil and see if the higher-order stencil actually produces more accurate results. Figure 5.5 shows the spectrum resulting from each stencil with $N = 128$ at the time that $a = 6.7$ (i.e. roughly the moment at which the simulation is not expected to be accurate anymore) and $a = 13.45$. Both simulations show good agreement, but using the isoC stencil seems to generally result in a greater value of the spectrum for $k_p/H_i \geq 10^3$ and seems to diverge faster at $k_p/H_i \approx 10^3$. It, therefore, seems that using the isoD stencil will give more accurate results.

Directional derivatives

Instead of changing the stencil for the calculation of the Laplacian, the stencil for calculating the directional derivatives that then source the GWs can also be changed. Figure 5.6 shows the results of using the isoD stencil in combination with either a 4th order stencil or an 8th order stencil for the directional derivative. The spectra are again shown at $a = 6.7$ and $a = 13.45$ for $N = 128$. Both stencils show good agreement, only slightly differing for $k_p/H_i \geq 2 \times 10^3$ and at $k_p/H_i \approx 10^3$, where the simulation with the 8th order stencil seems to result in a slightly lower peak. In comparison to changing the Laplace stencil, the change here does not seem to be significant.

TT projection

Figure 5.7 shows how the custom lattice TT projector (which uses the effective lattice momentum in eq. 4.3.10) compares to the continuum projector. Both spectra were obtained from a simulation with $N = 128$, the 4th order accurate directional derivative, and the isoD stencil. The continuum projector features a more pronounced peak at the high end of the spectrum for $a = 6.7$, indicating that the TT projector does not completely remove all non-TT components of the spectrum. Using the custom TT projector seems to generally give more accurate results.

Further, the left panel in fig. 5.8 compares the not TT projected to the TT projected GW spectrum. Also shown are gray dashed lines that correspond to multiples of $1/(m_\phi H_i)$, i.e. the harmonics of the oscillons. As can be seen, the not projected spectrum has more features corresponding to the oscillon harmonics, which however get lost by TT projecting. The right panel further compares the effective EMT with the TT projected one. Again, we can see that TT projecting removes the oscillon features almost completely.
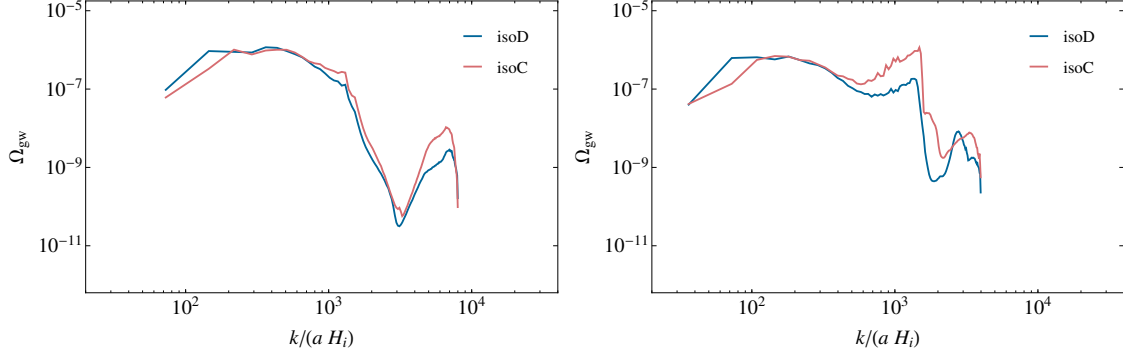
Figure 5.5.: GW spectra obtained with the isoD and isoC stencil by using the custom TT projector and $N = 128$. Displayed at $a = 6.7$ (left) and $a = 13.45$ (right).
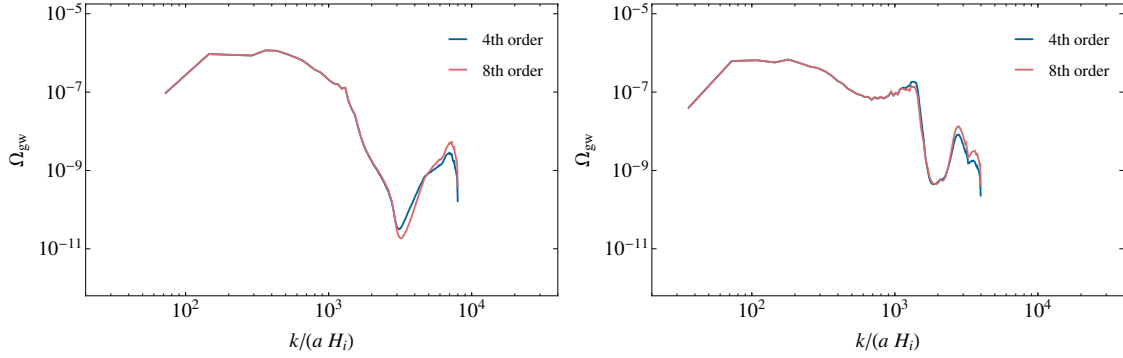

Figure 5.6.: GW spectrum obtained with an 4th and 8th order stencil for the directional derivatives by using the custom TT projector and $N = 125$. Both simulations use $N = 128$ and are displayed at $a = 6.7$ (left) and $a = 13.45$ (right).
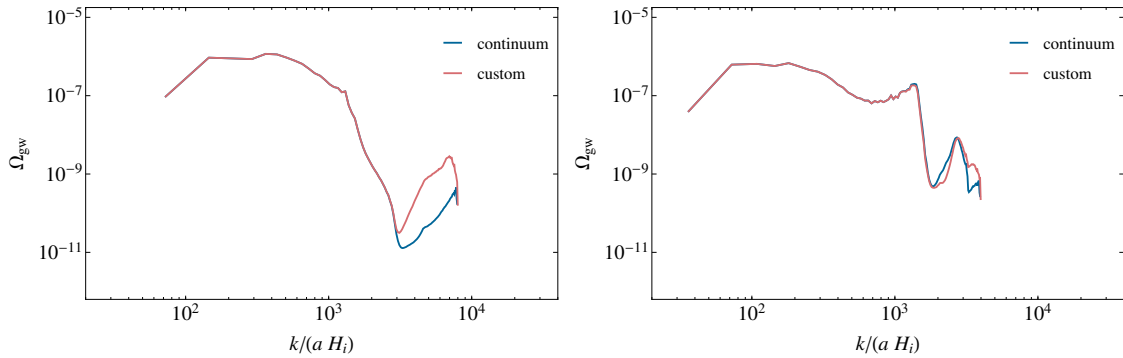

Figure 5.7.: GW spectrum obtained with the continuum projector and the custom lattice projector. Both simulations use $N = 128$ and are displayed at $a = 6.7$ (left) and $a = 13.45$ (right).
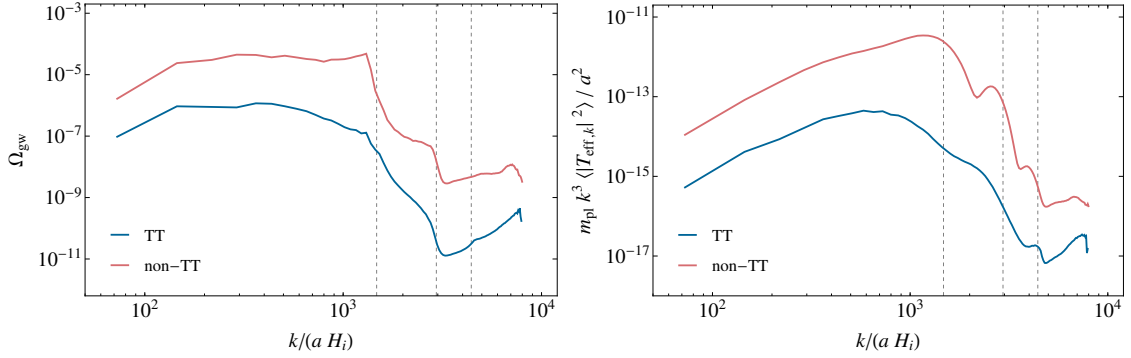
Figure 5.8.: TT project and raw spectra for the GW spectrum (left) and EMT (right). Both at $a = 6.7$ with $N = 128$.

5.2. Hilltop model

In the following, I will summarize the results of simulating the GWs in the hilltop model, where the inflaton couples to an additional scalar field. This model was shown to be compatible with inflation, as such that its resulting spectral index and tensor perturbations are in agreement with the most recent bounds from cosmic microwave background measurements provided by PLANCK [37]. See [13] for motivations and details on this model. The specific potential that was investigated is of the following form:

$$V(\phi, \chi) = V_0 \left(1 - \frac{\phi^6}{v^6}\right)^2 + \frac{\lambda^2}{2}\phi^2\chi^2(\phi^2 + \chi^2), \qquad (5.2.3)$$

where ϕ takes the role of the inflaton and χ is the additional scalar field that couples to it. As already discussed before, this potential features tachyonic modes for the inflaton that will grow exponentially. In [64] it was shown that this potential also features parametric resonance of χ for certain values of λ after oscillons have already formed. This resonance was shown to occur for $0.7 \times 10^{-3} \leq \lambda\,m_{\mathrm{pl}} \leq 1.4 \times 10^{-3}$. The authors also found that couplings outside of this resonance band do not have a significant effect on the evolution of oscillons. In the following I will therefore specifically consider the values $\lambda\,m_{\mathrm{pl}} = 1.0 \times 10^{-3}$, 1.2×10^{-3} and 1.3×10^{-3}. The GWs produced in these cases might be interesting since the second field could possible introduce new features in the GW spectra.

Figure 5.9 shows in its left panel the total GW spectra, as well as the GW spectra only of the χ field at end of the simulation $a = 9$ with $N = 128$. Note that we now have $dx \approx 0.11/m_\phi$, meaning that the simulations are still trustworthy at this

$v/m_{\rm pl}$	$V_0/m_{\rm pl}^4$	$m_\phi/m_{\rm pl}$	$H_i/m_{\rm pl}$	$L\,H_i$	N	$dt\,m_\phi$
10^{-2}	10^{-19}	2.68×10^{-7}	1.9×10^{-10}	0.1	128	0.02

$\phi_i/m_{\rm pl}$	$\dot{\phi}_i/m_{\rm pl}^2$	$\chi_i/m_{\rm pl}$	$\dot{\chi}_i/m_{\rm pl}^2$
$0.08v$	$2.49 \times 10^{-9}v^2$	0	0

Table 5.3.: Parameter used for the simulation of the model with potential shown in eq. 5.2.3. For more information see the original work in [13].
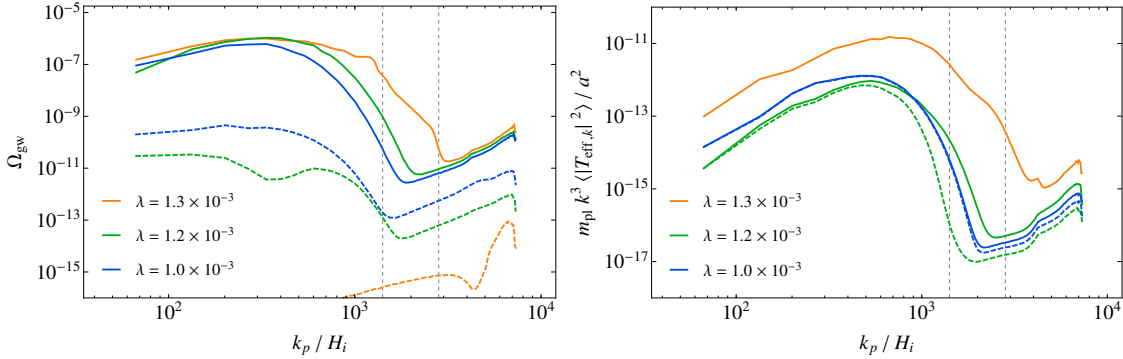

Figure 5.9.: GW spectrum (left) and spectrum of the TT projected EMT (right) for different values of λ, which are shown in the panels in units of $m_{\rm pl}^{-1}$. Continuous lines indicate the full spectra (both scalar fields are included) and the colored dashed lines indicate the spectra of only the χ field. The dashed gray lines indicate values at which $k_p = m_\phi$ and $k_p = 2m_\phi$. Both figures are created at $a = 9$ with $N = 128$.

scale factor. As can be seen, the total GW spectrum becomes weaker for values of λ closer to $\lambda = 1.0 \times 10^{-3}/m_{\rm pl}$, indicating that the additional field does rather weaken the spectrum, instead of enhancing it. Further, it can be seen that for $\lambda = 1.0 \times 10^{-2}/m_{\rm pl}$ and $1.2 \times 10^{-2}/m_{\rm pl}$, the spectrum does not seem to include the features that were previously visible at roughly the positions of the oscillon harmonics (see fig. 5.8). Only for $\lambda = 1.3 \times 10^{-3}/m_{\rm pl}$ these features are visible, but red-shifted. This indicates, that the oscillons already decayed early in the simulation and did thus not source any significant amount of GWs henceforth. In the case for $\lambda = 1.3 \times 10^{-3}/m_{\rm pl}$, the situation is such that a certain amount of GWs were sourced by the oscillons, but after parametric resonance started, the oscillons decayed. In the shown spectrum for the χ field, we can see that it does not catch any significant features from the oscillons, instead, it is always at least one order of magnitude
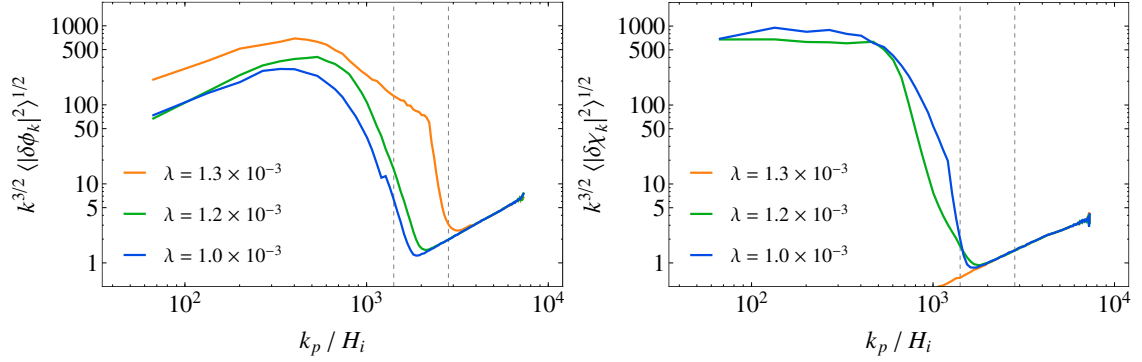
Figure 5.10.: Spectrum of field perturbation for ϕ (left) and χ (right) for different values of λ, which are shown in the panels in units of m_{pl}^{-1}. The dashed gray lines indicate values at which $k_p = m_\phi$ and $k_p = 2m_\phi$. Both figures are created at $a = 9$ with $N = 128$.

weaker than the total GW spectrum.

The right panel in fig. 5.9 shows the TT projected effective EMT, which further strengthens the above discussion: Non of the typical oscillon features are visible for the smaller values of λ and only $\lambda = 1.3 \times 10^{-3}/m_{\mathrm{pl}}$ hints at oscillons that existed at previous points in the simulation. Also, the figure shows that, in the case of the smaller values for λ, the EMT spectrum is dominated by the χ field for smaller momenta ($k_p/H_i \leq 700$). However, for $\lambda = 1.3 \times 10^{-3}/m_{\mathrm{pl}}$ the χ field does not source any significant amount of GW at all and is thus not visible in the figure.

Figure 5.10 shows the spectrum of field perturbation for both fields and considered values of λ. The spectra shapes are comparable to those of the GWs, which were discussed above. Again, when the χ field is significantly excited by parametric resonance, then the spectrum of the ϕ field is weakened. Also, in the case of $\lambda = 1.3 \times 10^{-3}/m_{\mathrm{pl}}$, the χ field does not show any significant amplification.
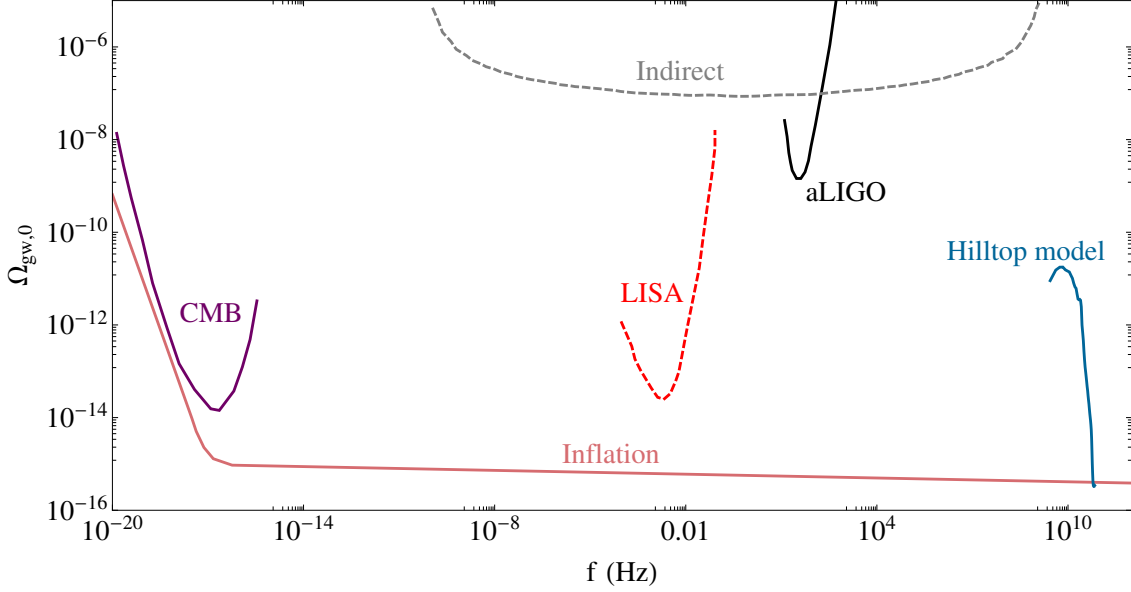
6. Summary and outlook

Figure 6.1.: Shown are the expected sensitivity curves of the fifth observing run of the aLIGO network [65] and the planned space-based observatory LISA [66]. Also shown are constraints arising from CMB measurements [37] and indirect limits, also resulting from the CMB [67]. An upper limit for the GW spectrum resulting from slow-roll inflation is shown, where a tensor-to-scalar ratio of $r = 0.11$ was used, which is consistent with PLANCK measurements [37]. Finally, the spectrum resulting from reheating in the Hilltop model with an additional scalar field is shown for $\lambda = 1.3 \times 10^{-3}/m_{\rm pl}$ (orange curve in fig. 5.9). The GW spectrum was red-shifted using $h = 0.72$ together with eq. 2.1.35 and 2.1.36.

In this thesis, the numerical subtleties of performing lattice simulations that aim to evolve GWs sourced by one, or multiple scalar fields were discussed. Also, new GPU accelerated code was developed that can use different stencils for the necessary spatial derivatives. Especially, a 4th order accurate and 6th order isotropic stencil for the Laplacian was introduced that performs better than the standard nearest

6. Summary and outlook

neighbor stencil, but not as good as the pseudospectral method. The developed code was applied to a model that features a hilltop potential for the inflaton and is additionally coupled to another scalar field. However, it was found that the GWs produced by oscillons in this model do not leave a significant imprint on the total GW spectrum, which in turn is dominated by a background produced due to tachyonic resonance. Also, as fig. 6.1 illustrates, the produced spectrum is in a frequency area that is multiple orders of magnitude larger than what is measurable with current technology. This placement is typical for reheating after large-scale inflation [16], meaning that it will be necessary to develop new technology or methods to access this area.

Nonetheless, while single oscillons do not (or only barely) radiate GWs due to their spherical nature, systems of oscillons are generally still expected to result in the production of GWs via processes such as the merging of two oscillons. Since these processes generally require simulating the gravitational interaction between oscillons, the simulations become more complicated, especially since gravitation typically acts on larger time scales than oscillons do. This area has only recently started to be explored (see e.g. [68, 69]).

A measurement of the GWs background will help us to gain a deeper understanding not only of processes that take place during reheating but also of other important points such as dark matter and dark energy. The upcoming GW observatories, such as DECIGO [70] and LISA [66], are therefore of great importance to the field of cosmology.

A. Lattice simulation

In this appendix, I aim to explain the steps taken to ensure that the written simulation provides accurate data, while still having an endurable execution time. I will first explain the used field rescalings, how the Laplacian is calculated by using finite difference stencils, and afterward I will go into detail on the CUDA platform and the way that the field evolution is implemented. Finally, I will give a few remarks on the usage of single and double-precision.

A.1. Rescalings

I will make use of the variable rescalings that are already implemented in LatticeEasy [58]. Specifically, the following rescalings are used:

$$f_{\mathrm{pr}} = a^r f / f_0, \quad \mathbf{x}_{\mathrm{pr}} = m_f \mathbf{x}, \quad dt_{\mathrm{pr}} = m_f a^s dt, \tag{A.1.1}$$

where subscripts of pr denote the variables in program units, f denotes the scalar field that is to be simulated, f_0 its initial value and m_f its mass. Additionally, the constraint $s - 2r + 3 = 0$ needs to be fulfilled, which will eliminate the term proportional to $\dot{f}$ in the equation of motion (see eq. 2.1.8), which then have the shape of

$$f_{\mathrm{pr}}'' - a^{-2s-2} \Delta_{\mathrm{pr}} f_{\mathrm{pr}} - \left(r(s - r + 2) H_{\mathrm{pr}}^2 + r \frac{a''}{a} \right) f_{\mathrm{pr}} + \frac{dV_{\mathrm{pr}}}{df_{\mathrm{pr}}} = 0, \tag{A.1.2}$$

where primes denote derivatives with respect to dt_{pr} and

$$V_{\mathrm{pr}}(f_{\mathrm{pr}}) = \frac{1}{m_f^2 f_0^2} a^{-2s+2r} V(f_{\mathrm{pr}}). \tag{A.1.3}$$

The same rescalings are used for the tensor perturbations, except that $h_{ij,\mathrm{pr}} = a^r h_{ij} / f_0^2$,

which simplifies the equations of motion (see eq. 4.4.12) to

$$h_{\mathrm{pr}}'' - a^{-2s-2}\Delta_{\mathrm{pr}}h_{\mathrm{pr}} - \left(r(s-r+2)H_{\mathrm{pr}}^2 + r\frac{a''}{a}\right)h_{\mathrm{pr}} = 2a^{-2s-r-2}T_{\mathrm{pr}}^{\mathrm{eff}}, \qquad \text{(A.1.4)}$$

with $h_{\mathrm{pr}} \equiv h_{ij,\mathrm{pr}}$ and

$$T_{ij,\mathrm{pr}}^{\mathrm{eff}} = m_f^2 f_0^2 a^{2r} T_{ij}^{\mathrm{eff}} = \partial_{i,\mathrm{pr}}f_{\mathrm{pr}}\partial_{j,\mathrm{pr}}f_{\mathrm{pr}}. \qquad \text{(A.1.5)}$$

A.2. Finite difference stencils

The differential equation which is to be solved depends on the Laplacian of the field at each grid point, not only for the considered scalar fields but also for each component of the tensor perturbations. The usual approach for obtaining this value is to employ finite difference methods: Multiply the value of the grid points in direct proximity with a weight and sum the results. For a function f which is defined on the grid, this takes the form of

$$\Delta f(x,y,z) \approx \sum_{ijk} S_{ijk} f(x+ih, y+jh, z+kh), \qquad \text{(A.2.6)}$$

where S_{ijk} is called the stencil and h is the grid spacing. If the error to the exact value is of order h^n, then the respective stencil is called an nth order stencil. Typically, a 7-point stencil is used to approximate the Laplacian, which only utilizes the 6 nearest neighbors, as well as the central point (thus *7-point* stencil). For this stencil, the truncation error is of order $\mathcal{O}(h^2)$, but will be dependent on the direction, which will cause inhomogeneities to propagate in an anisotropic manner. By using all the points that surround the grid point which is of interest, it is however possible to construct stencils that are still second-order accurate, but 4th order isotropic. In [17] it was noted that the usual 2nd order nearest neighbor stencil can lead to the production of unwanted artifacts. In order to ensure good quality of the simulated data, I constructed a stencil that is 4th order accurate and 6th order isotropic[1]. In the following, I will describe the general procedure to construct such stencils, which is taken from [59].

---

[1]Meaning that, if this stencil is applied to an arbitrary polynomial, the truncation error up to order $\mathcal{O}(h^6)$ is independent on the orientation of the polynomial.
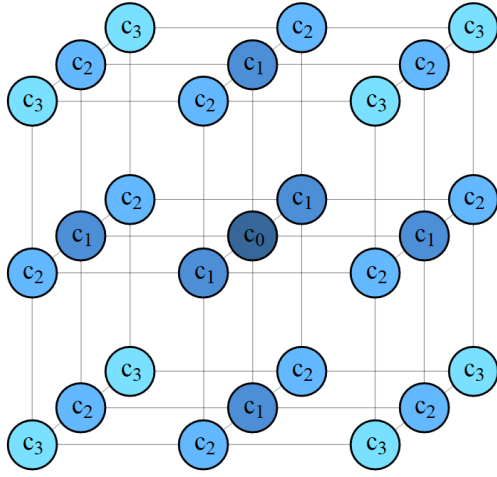
coefficient	c_3	c_2	c_1	$-c_0$	$\alpha >$
standard	0	0	1	6	$\sqrt{3}$
isotropic A	0	$\frac{1}{6}$	$\frac{1}{3}$	4	$\sqrt{2}$
isotropic B	$\frac{1}{12}$	0	$\frac{2}{3}$	$\frac{14}{3}$	$\frac{\sqrt{21}}{3}$
isotropic C	$\frac{1}{30}$	$\frac{1}{10}$	$\frac{7}{15}$	$\frac{64}{15}$	$\frac{8}{\sqrt{30}}$

Figure A.1.: A general 27 point stencil for the calculation of the Laplacian. Due to the symmetry of the Laplacian, the stencil also needs to have the same symmetry reducing the amount of coefficients to four.

A.2.1. Isotropic stencils

Let S be an nth order stencil to a given differential operator $\mathcal{D}$ of order p, then the stencil should give exact results for any polynomial of order $q = p + n - 1$. This means we have

$$\sum_{ijk} S_{ijk} P_q(x + ih, y + ih, z + ih) = \mathcal{D}P_q(x, y, z), \quad \text{for} \quad \sum_{i,j,k=0,...,q}^{i+j+k \leq q} a_{ijk} x^i y^j z^k. \quad \text{(A.2.7)}$$

Using the above equation will result in a stencil that is accurate to the desired order, but not necessarily isotropic. For the Laplacian, an additional condition will therefore be that the leading term of the truncation error is proportional to an appropriate power of the Laplacian itself.[2] Figure A.1 shows the distribution of a general 2nd order stencil for the Laplacian. The stencil for the Laplacian includes an overall factor of h^{-2} which I will however not explicitly write out in the following for every coefficient in order to ease the notation. To fulfill eq. A.2.7, the coefficients need to have the following relation

$$c_1 = 1 - 4c_3 - 4c_2, \quad c_0 = 16c_4 + 12c_2 - 6. \quad \text{(A.2.8)}$$

---

[2]Note that this is equivalent to rotating the input function and demanding that appearing terms of sinus and cosinus cancel.
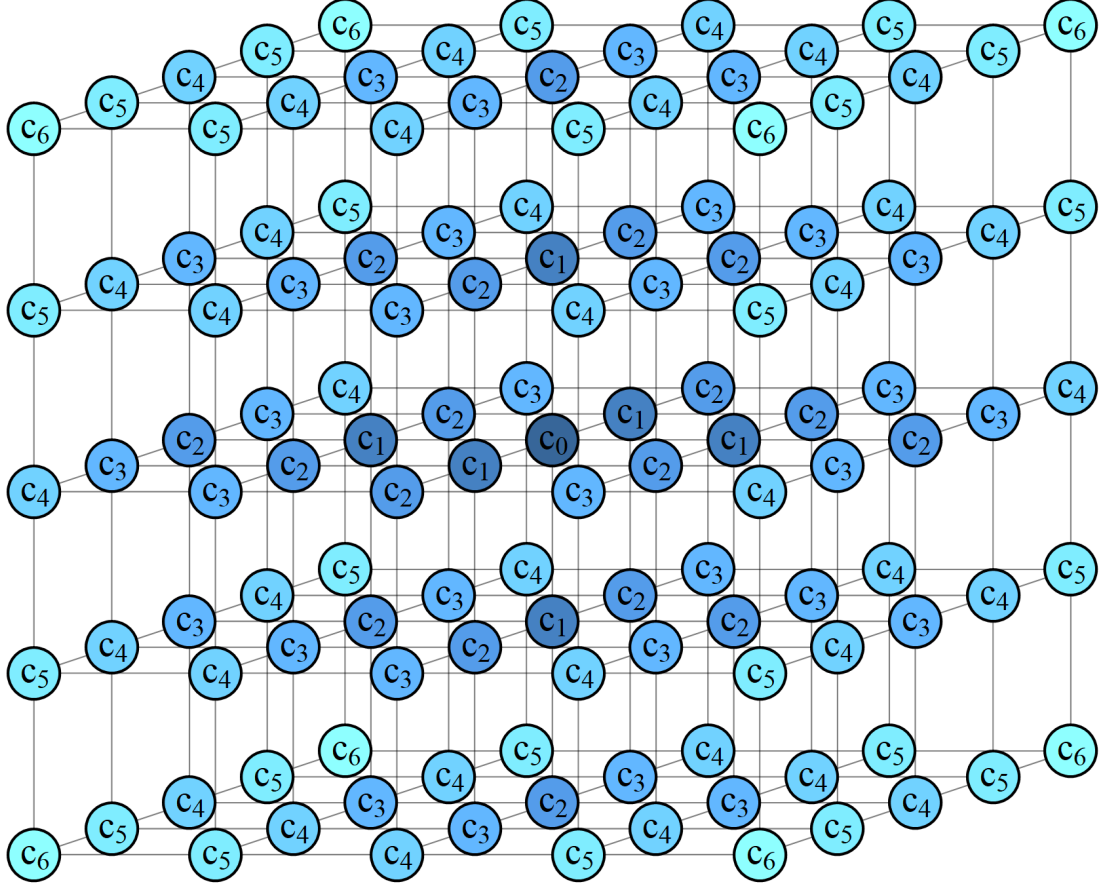
Figure A.2.: Here used version of a 5^3 point stencil.

When additionally demanding the stencil to be isotropic to 4th order we obtain

$$c_2 = \frac{1}{6} - 2c_3, \quad c_1 = \frac{1}{3} + 4c_3, \quad c_0 = -4 - 8c_3. \tag{A.2.9}$$

Note that there is still one free parameter that can be chosen to ensure optimal stability for the considered differential equation (see next section).

For the attempt of constructing a 4th order accurate isotropic stencil, we should now also consider the neighbors of the neighboring grid points, i.e. we extend the stencil by an additional layer, meaning that it now consists of 5^3 points (see fig. A.2). Due to symmetry arguments, we would in general need ten coefficients to describe the general 5^3-point stencil, however, by already demanding a particular coefficient distribution beforehand this number can be reduced to seven. The distribution I was interested in is designed such that the stencil value depends on how many steps were taken from the origin: The origin itself has coefficient c_0, while doing e.g. a step

to either side and then upwards results in c_2, the same value as doing directly two steps in any direction. This stencil shape is shown in fig. A.2. This shape has the advantage of being particularly easy to implement in a way that will reduce reads to the memory where these coefficients are stored, thus improving the simulation speed. Again, by demanding eq. A.2.7 to be fulfilled, we obtain the following requirements for the stencil coefficients

$$
\begin{aligned}
c_6 &= \frac{1}{192}\left(212 + 24c_0 - 3c_1\right), \quad c_5 = 0, \quad c_4 = \frac{1}{48}\left(-98 - 12c_0 - 3c_1\right), \\
c_3 &= \frac{1}{96}\left(356 + 48c_0 + 33c_1\right), \quad c_2 = -\frac{1}{16}\left(48 + 8c_0 + 13c_1\right).
\end{aligned}
\tag{A.2.10}
$$

Further, the stencil is isotropic to 6th order if $c_1 = 52/25$. Note that, again, one free coefficient, c_0, is left. In the next section, I will perform a stability analysis that will reveal an appropriate value for this coefficient. If we had instead used the more general shape of this stencil with 5^3 points, then the extra coefficients could have been chosen in order to achieve it being isotropic up to 8th order. However, as mentioned above, the interest does not only lie in optimizing accuracy, but also in optimizing execution time, which favors the restricted stencil that was constructed above.

A.2.2. Von Neumann stability analysis

So far only the discretization error was considered while deriving the stencil coefficients. Minimizing this error will however not guarantee that the stencil is actually suitable for use in a simulation. Even if a stencil has a truncation error of $\mathcal{O}(h^4)$, it can lead to unstable behavior, such that certain modes on the lattice receive non-physical growth and thus invalidate the simulation. In the following, I will discuss how stability can be ensured and derive a value for the last free parameter of the 5^3-point stencil from this condition. This can be done by doing a Von Neumann analysis: Decompose the considered field f into Fourier modes and test under what conditions the amplitudes of all modes have appropriate behavior (i.e. the amplitudes should not experience nonphysical growth). In order to do this, I will first write down the used time integration scheme and then explicitly derive the condition for stability.

The program uses the already implemented staggered leapfrog scheme that is

accurate to second order in time. Explicitly, the time integration is done such that

$$
\begin{aligned}
f(t) &= f(t - dt) + dt\,\dot{f}(t - dt/2) \\
\dot{f}(t + dt/2) &= \dot{f}(t - dt/2) + dt\,\ddot{f}(t) \\
f(t + dt) &= f(t) + dt\,\dot{f}(t + dt/2)
\end{aligned}
\tag{A.2.11}
$$

$$\dots$$

We can collapse this scheme to obtain

$$
\frac{f(t + dt) + f(t - dt) - 2f(t)}{dt^2} = \ddot{f}(t),
\tag{A.2.12}
$$

where the second order nature is now revealed. The full form of $\ddot{f}$ is given in eq. A.1.2, I will here however only consider the Laplacian part and rescale the space coordinates, such that $\ddot{f}(t) = \Delta f$. The dependence on the scale factor will later be reintroduced. The general Solution to the (non-discretized) differential equation is given by

$$
u(t, \mathbf{x}) = e^{i(\mathbf{k}\cdot\mathbf{x} \pm \omega t)}
\tag{A.2.13}
$$

The analysis is therefore usually done by using the ansatz

$$
u(n, \mathbf{p}) = \chi^n e^{i\,dx\,\mathbf{k}\cdot\mathbf{p}},
\tag{A.2.14}
$$

where I used that $t = n\,dt$ and $\mathbf{p}$ represents the position vector on the grid. Also, from here on I will denote the grid spacing with dx. The Laplacian is then given by

$$
\Delta u(n, \mathbf{p}) = \chi^n \sum_{\mathbf{q}} S_{\mathbf{q}} e^{i\,dx\,\mathbf{k}\cdot(\mathbf{p}+\mathbf{q})} = u(n, \mathbf{p}) \sum_{\mathbf{q}} S_{\mathbf{q}} e^{i\,dx\,\mathbf{k}\cdot\mathbf{q}}
\tag{A.2.15}
$$

Combining the above equation together with eq. A.2.12 then results in

$$
\frac{\chi^{n+1} + \chi^{n-1} - 2\chi^n}{dt^2} = \frac{\chi^n}{dx^2} \underbrace{\sum_{\mathbf{q}} S_{\mathbf{q}} e^{i\,dx\,\mathbf{k}\cdot\mathbf{q}}}_{\Delta_S :=}
\tag{A.2.16}
$$

Note that I put the overall factor of dx^{-2} of the stencil in front of the sum. The

above equation can be solved exactly such that

$$\chi = 1 + \frac{\Delta_S}{2\alpha^2} \pm i\sqrt{1 - \left(1 + \frac{\Delta_S}{2\alpha^2}\right)^2}, \tag{A.2.17}$$

with $\alpha = dx/dt$. It becomes evident now that in order to guarantee that no mode experiences nonphysical amplification (i.e. $|\chi|^2 = 1$) it is necessary that

$$\left(1 + \frac{\Delta_S}{2\alpha^2}\right)^2 \leq 1, \tag{A.2.18}$$

or equivalently

$$0 \leq -\frac{\Delta_S}{4} \leq \alpha^2. \tag{A.2.19}$$

We therefore have to find the extrema of Δ_S, which is a nontrivial task. However, there is a convenient approximation that we can use:

$$c_0 - |c_0| \leq \Delta_S \leq c_0 + |c_0|, \tag{A.2.20}$$

where I used that

$$\sum_{\mathbf{q}} S_{\mathbf{q}} = 0. \tag{A.2.21}$$

The above inequality reveals that the 5^3-point stencil is stable for $c_0 = -177/20$. In summary, all coefficients are given by

$$c_0 = -\frac{177}{20}, \quad c_1 = \frac{52}{25}, \quad c_2 = -\frac{53}{200}, \quad c_3 = -\frac{1}{600}, \\ c_4 = \frac{49}{1200}, \quad c_5 = 0, \quad c_6 = -\frac{83}{2400}. \tag{A.2.22}$$

Also, the stencil is stable for $\alpha = a^{2s+2} dx/dt \geq 2.46$.

A.3. CUDA programming

Compute Unified Device Architecture (CUDA) is a platform developed by Nvidia that enables programs to make general use of graphics processing units (GPUs) that were also developed by Nvidia. In the following, I will explain why CUDA is a
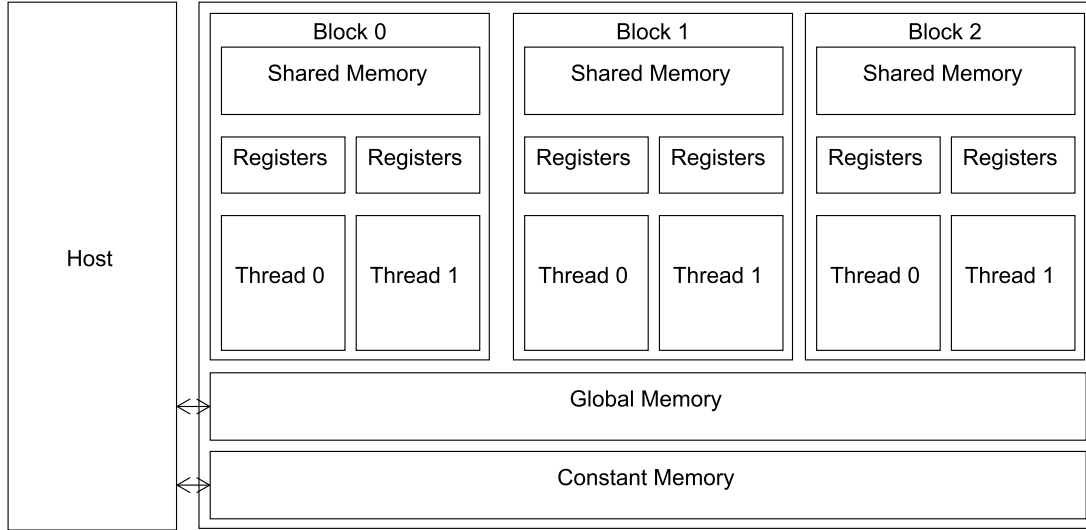
Figure A.3.: Simplified overview of memory types and their relation to threads and thread blocks. For more information see [19].

sensible choice for the simulations that were done for this work, and I will also explain the implementation strategy that I followed in order to optimize performance.

A.3.1. Overview

A usual modern central processing unit (CPU) can run a few threads, typically in the range of 4 to 16, in parallel (i.e. it can handle this many instructions in parallel), a typical modern GPU however can run multiple thousands of threads in parallel. In this work, I investigated the evolution of scalar fields, a task that is well suited to be done in parallel, as the instructions that are applied to each grid point are the same. Programs of this sort are most often parallelized using multiple CPUs and distribute the workload accordingly. However, as already mentioned, a single GPU can often already offer more potential than multiple CPUs.

The memory management becomes rather delicate when using a GPU, since there are multiple levels of memory that have to be utilized in the correct way, otherwise stalling the performance. Figure A.3 shows a simplified overview of available memory on the various levels. In general, CUDA distributes the workload across thread blocks, which each have a fixed amount of threads. At the ground level we have the global memory, a memory space that can be accessed from the CPU, as well as the GPU, but having the caveat that reads and writes from and to global memory takes

rather long. While global memory can be accessed from every thread in every thread block, the shared memory is specific to each thread block but is of less size. While shared memory is, therefore, more restrictive, reads and writes are a lot faster than global memory. Each thread also has an assigned register, where the local variables are stored, which also offers the fastest access. Constant memory is only readable from the GPU and offers speed similar to registers but only if all threads read the same address from constant memory at the same time.

Hence, the strategy is to put all variables that are the same for all threads (such as the scale factor) into constant memory. When calculating the Laplacian, each thread block will load all values of the field into shared memory that its threads need to calculate the Laplacian for all covered points (see also next section).

A.3.2. Implementation

The fields are evolved using the same workflow as LatticeEasy already uses:

1. evolve the scale factor

2. evolve the value of the derivative of each field

3. evolve their field values

Since the first step is not suitable to be parallelized, I left it to be evaluated on the CPU. For the other two steps, the general strategy is to avoid bandwidth limitations by minimizing access to global memory. This is easily done for the update of the field values: I wrote the kernels such that one kernel is spawned for each lattice point, which then loads the field value and its derivative, adjusts the field value, and writes it back. The calculation of the derivative value is however more bothersome due to the necessity of calculating the Laplacian: Each grid point also needs the values of the neighboring lattice points to calculate the Laplacian. Instead of again spawning one thread for each grid point and having each thread also load the value of its neighbors, it is advisable to use a slab decomposition, which is described in detail in [71]. The strategy is visualized in fig. A.4. The $z = 0$ layer is divided into multiple groups that will each correspond to one thread block. Then, one thread is spawned for each point in each group. In order to minimize the access to global memory, each group will load all values that are necessary to calculate the stencil for each of its points into their shared memory. Specifically, the next values in the
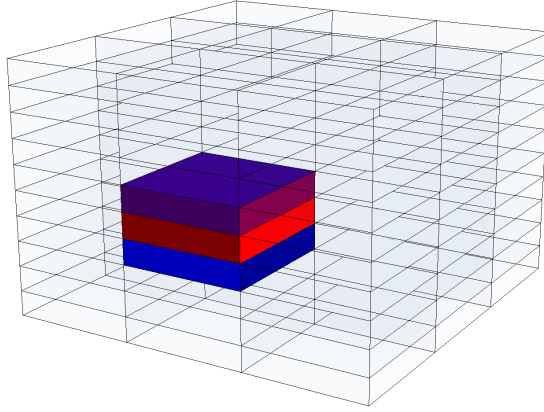
Figure A.4.: Schematics of the slab decomposition for a lattice of size $N = 10^3$: Each block in a $z = $ const layer represents a thread block. The colored slabs are the values that are stored in the shared memory of the thread group that is currently at the position of the red block. In the next step, the purple block will replace the red block, the next block is loaded and the blue block is discarded.

positive z-direction and the previous values in the opposite z-direction are always necessary. If the derivatives on one layer are calculated, then the values that are stored in the shared memory are all shifted into the negative z-direction and the next layer in the positive z-direction is loaded into shared memory. In this way, it is only necessary to iterate once over the grid and the access to global memory is efficiently handled.

A.3.3. Single vs double-precision

Since the typical GPU can handle calculations in single-precision significantly faster than in double-precision, it is favorable to adjust the simulation in such a way that single-precision captures the dynamics similarly well as double-precision. Due to the non-associative nature of floating-point operations, this however becomes a nontrivial task. Imagine for example having an array of single-precision numbers that start with the number 1 and is followed by an arbitrary amount of numbers with value 10^{-10}, i.e. $(1, 10^{-10}, \ldots, 10^{-10})$. If single-precision is used and the array is summed by starting at the first number and then sequentially adding the next, it

would result in simply 1 as the total sum, independent of how many elements are in the list. While this example is an extreme case, the precision loss of obtaining the mean energy density on the lattice can become quite large. The test runs that I did differed by roughly four orders of magnitude when comparing single-precision to double-precision runs. The program instead utilizes a parallel reduction method: The first two elements in an array are summed and stored, then the third and fourth elements are summed and stored and so on, thus creating a new array of half the length, where the same procedure is recursively applied until one obtains the sum of all elements. While there are also other methods, such as Kahan summation that also lead to a precision improvement, I found that the parallel reduction method provides the best agreement between single and double-precision.

Bibliography

[1] M. A. Amin, R. Easther, and H. Finkel, "Inflaton Fragmentation and Oscillon Formation in Three Dimensions," *JCAP* **12** (2010) 001, `arXiv:1009.2505 [astro-ph.CO]`.

[2] A. V. Frolov, "Non-linear Dynamics and Primordial Curvature Perturbations from Preheating," *Class. Quant. Grav.* **27** (2010) 124006, `arXiv:1004.3559 [gr-qc]`.

[3] M. A. Amin, J. Fan, K. D. Lozanov, and M. Reece, "Cosmological dynamics of Higgs potential fine tuning," *Phys. Rev. D* **99** no. 3, (2019) 035008, `arXiv:1802.00444 [hep-ph]`.

[4] J.-F. Dufaux, D. G. Figueroa, and J. Garcia-Bellido, "Gravitational Waves from Abelian Gauge Fields and Cosmic Strings at Preheating," *Phys. Rev. D* **82** (2010) 083518, `arXiv:1006.0217 [astro-ph.CO]`.

[5] S. Antusch, F. Cefalà, and F. Torrentí, "Properties of Oscillons in Hilltop Potentials: energies, shapes, and lifetimes," *JCAP* **10** (2019) 002, `arXiv:1907.00611 [hep-ph]`.

[6] J.-P. Hong, M. Kawasaki, and M. Yamazaki, "Oscillons from Pure Natural Inflation," *Phys. Rev. D* **98** no. 4, (2018) 043531, `arXiv:1711.10496 [astro-ph.CO]`.

[7] N. Graham and N. Stamatopoulos, "Unnatural Oscillon Lifetimes in an Expanding Background," *Phys. Lett. B* **639** (2006) 541–545, `arXiv:hep-th/0604134`.

[8] E. Cotner, A. Kusenko, and V. Takhistov, "Primordial Black Holes from Inflaton Fragmentation into Oscillons," *Phys. Rev. D* **98** no. 8, (2018) 083513, `arXiv:1801.03321 [astro-ph.CO]`.

[9] D. Bazeia, A. R. Gomes, K. Nobrega, and F. C. Simas, "Oscillons in hyperbolic models," *Phys. Lett. B* **803** (2020) 135291, `arXiv:1911.03352 [hep-th]`.

[10] G. Fodor, *A review on radiation of oscillons and oscillatons.* PhD thesis, Wigner RCP, Budapest, 2019. `arXiv:1911.03340 [hep-th]`.

[11] S. Antusch, F. Cefala, S. Krippendorf, F. Muia, S. Orani, and F. Quevedo, "Oscillons from String Moduli," *JHEP* **01** (2018) 083, `arXiv:1708.08922 [hep-th]`.

[12] E. Farhi, N. Graham, V. Khemani, R. Markov, and R. Rosales, "An oscillon in the $su(2)$ gauged higgs model," *Phys. Rev. D* **72** (Nov, 2005) 101701. `https://link.aps.org/doi/10.1103/PhysRevD.72.101701`.

[13] S. Antusch and S. Orani, "Impact of other scalar fields on oscillons after hilltop inflation," *JCAP* **03** (2016) 026, `arXiv:1511.02336 [hep-ph]`.

[14] S.-Y. Zhou, E. J. Copeland, R. Easther, H. Finkel, Z.-G. Mou, and P. M. Saffin, "Gravitational Waves from Oscillon Preheating," *JHEP* **10** (2013) 026, `arXiv:1304.6094 [astro-ph.CO]`.

[15] S. Antusch, F. Cefala, and S. Orani, "What can we learn from the stochastic gravitational wave background produced by oscillons?," *JCAP* **03** (2018) 032, `arXiv:1712.03231 [astro-ph.CO]`.

[16] M. A. Amin, M. P. Hertzberg, D. I. Kaiser, and J. Karouby, "Nonperturbative Dynamics Of Reheating After Inflation: A Review," *Int. J. Mod. Phys. D* **24** (2014) 1530003, `arXiv:1410.3808 [hep-ph]`.

[17] S. Antusch, F. Cefala, and S. Orani, "Gravitational waves from oscillons after inflation," *Phys. Rev. Lett.* **118** no. 1, (2017) 011303, `arXiv:1607.01314 [astro-ph.CO]`. [Erratum: Phys.Rev.Lett. 120, 219901 (2018)].

[18] M. A. Amin, J. Braden, E. J. Copeland, J. T. Giblin, C. Solorio, Z. J. Weiner, and S.-Y. Zhou, "Gravitational waves from asymmetric oscillon dynamics?," *Phys. Rev. D* **98** (2018) 024040, `arXiv:1803.08047 [astro-ph.CO]`.

[19] NVIDIA, P. Vingelmann, and F. H. Fitzek, "Cuda, release: 11.2.1," 2021. `https://developer.nvidia.com/cuda-toolkit`.

[20] S. Weinberg, *Cosmology.* OUP Oxford, 2008.
https://books.google.de/books?id=rswTDAAAQBAJ.

[21] C.-P. Ma and E. Bertschinger, "Cosmological perturbation theory in the
synchronous versus conformal Newtonian gauge," arXiv:astro-ph/9401007.

[22] C. Caprini and D. G. Figueroa, "Cosmological Backgrounds of Gravitational
Waves," *Class. Quant. Grav.* **35** no. 16, (2018) 163001, arXiv:1801.04268
[astro-ph.CO].

[23] E. W. Kolb and M. S. Turner, *The early universe.* Frontiers in Physics.
Westview Press, Boulder, CO, 1990. https://cds.cern.ch/record/206230.

[24] R. Easther and E. A. Lim, "Stochastic gravitational wave production after
inflation," *Journal of Cosmology and Astroparticle Physics* **2006** no. 04, (Apr,
2006) 010–010. http://dx.doi.org/10.1088/1475-7516/2006/04/010.

[25] J.-F. Dufaux, A. Bergman, G. Felder, L. Kofman, and J.-P. Uzan, "Theory
and numerics of gravitational waves from preheating after inflation," *Physical
Review D* **76** no. 12, (Dec, 2007) .
http://dx.doi.org/10.1103/PhysRevD.76.123517.

[26] A. H. Guth, "Inflationary universe: A possible solution to the horizon and
flatness problems," *Phys. Rev. D* **23** (Jan, 1981) 347–356.
https://link.aps.org/doi/10.1103/PhysRevD.23.347.

[27] A. H. Guth, "Inflation and eternal inflation," *Phys. Rept.* **333** (2000) 555–574,
arXiv:astro-ph/0002156.

[28] P. Helbig, "Is there a flatness problem in classical cosmology?," *Mon. Not.
Roy. Astron. Soc.* **421** (2012) 561–569, arXiv:1112.1666 [astro-ph.CO].

[29] K. Lake, "The Flatness problem and lambda," *Phys. Rev. Lett.* **94** (2005)
201102, arXiv:astro-ph/0404319.

[30] R. Dicke and P. Peebles, "The Big-Bang Cosmology: Enigmas and
Nostrums," *Cambridge University Press* (1979) .

[31] J. P. Preskill, "Cosmological production of superheavy magnetic monopoles,"
Phys. Rev. Lett. **43** (Nov, 1979) 1365–1368.
https://link.aps.org/doi/10.1103/PhysRevLett.43.1365.

[32] A. Vilenkin and E. S. Shellard, *Cosmic Strings and Other Topological Defects*. Cambridge University Press, 7, 2000.

[33] D. Baumann, "Inflation," in *Theoretical Advanced Study Institute in Elementary Particle Physics: Physics of the Large and the Small*, pp. 523–686. 2011. `arXiv:0907.5424 [hep-th]`.

[34] L. Senatore, "Lectures on Inflation," in *Theoretical Advanced Study Institute in Elementary Particle Physics: New Frontiers in Fields and Strings*, pp. 447–543. 2017. `arXiv:1609.00716 [hep-th]`.

[35] T. Damour and V. F. Mukhanov, "Inflation without slow roll," *Phys. Rev. Lett.* **80** (1998) 3440–3443, `arXiv:gr-qc/9712061`.

[36] B. A. Bassett, S. Tsujikawa, and D. Wands, "Inflation dynamics and reheating," *Rev. Mod. Phys.* **78** (2006) 537–589, `arXiv:astro-ph/0507632`.

[37] **Planck** Collaboration, Y. Akrami *et al.*, "Planck 2018 results. X. Constraints on inflation," `arXiv:1807.06211 [astro-ph.CO]`.

[38] K. D. Lozanov, "Lectures on Reheating after Inflation," `arXiv:1907.04402 [astro-ph.CO]`.

[39] R. Allahverdi, R. Brandenberger, F.-Y. Cyr-Racine, and A. Mazumdar, "Reheating in Inflationary Cosmology: Theory and Applications," *Ann. Rev. Nucl. Part. Sci.* **60** (2010) 27–51, `arXiv:1001.2600 [hep-th]`.

[40] J. Liu, Z.-K. Guo, R.-G. Cai, and G. Shiu, "Gravitational wave production after inflation with cuspy potentials," *Phys. Rev. D* **99** (May, 2019) 103506. `https://link.aps.org/doi/10.1103/PhysRevD.99.103506`.

[41] J. Liu, Z.-K. Guo, R.-G. Cai, and G. Shiu, "Gravitational wave production after inflation with cuspy potentials," *Phys. Rev. D* **99** no. 10, (2019) 103506, `arXiv:1812.09235 [astro-ph.CO]`.

[42] M. I. Tsumagari, "The Physics of Q-Balls," other thesis, 10, 2009.

[43] N. Graham, "An electroweak oscillon," *Phys. Rev. Lett.* **98** (Mar, 2007) 101801. `https://link.aps.org/doi/10.1103/PhysRevLett.98.101801`.

[44] N. Graham, "Numerical simulation of an electroweak oscillon," *Phys. Rev. D* **76** (Oct, 2007) 085017.
https://link.aps.org/doi/10.1103/PhysRevD.76.085017.

[45] R. Correa, L. Ospedal, W. de Paula, and J. Helayël-Neto, "Supersymmetry and Fermionic Modes in an Oscillon Background," *Phys. Lett. B* **780** (2018) 159–165, arXiv:1712.01603 [hep-th].

[46] R. Correa, R. da Rocha, and A. de Souza Dutra, "D-Oscillons in the Standard Model-Extension," *Phys. Rev. D* **91** no. 12, (2015) 125021, arXiv:1504.04038 [hep-th].

[47] E. Cotner, A. Kusenko, M. Sasaki, and V. Takhistov, "Analytic Description of Primordial Black Hole Formation from Scalar Field Fragmentation," *JCAP* **10** (2019) 077, arXiv:1907.10613 [astro-ph.CO].

[48] J. Ollé, O. Pujolàs, and F. Rompineve, "Oscillons and Dark Matter," *JCAP* **02** (2020) 006, arXiv:1906.06352 [hep-ph].

[49] S. L. Liebling and C. Palenzuela, "Dynamical Boson Stars," *Living Rev. Rel.* **20** no. 1, (2017) 5, arXiv:1202.5809 [gr-qc].

[50] S.-W. Su, S.-C. Gou, I.-K. Liu, A. S. Bradley, O. Fialko, and J. Brand, "Oscillons in coupled bose-einstein condensates," *Phys. Rev. A* **91** (Feb, 2015) 023631. https://link.aps.org/doi/10.1103/PhysRevA.91.023631.

[51] H.-Y. Zhang, M. A. Amin, E. J. Copeland, P. M. Saffin, and K. D. Lozanov, "Classical Decay Rates of Oscillons," arXiv:2004.01202 [hep-th].

[52] M. P. Hertzberg, "Quantum Radiation of Oscillons," *Phys. Rev. D* **82** (2010) 045022, arXiv:1003.3459 [hep-th].

[53] M. Gleiser, "Oscillons in scalar field theories: Applications in higher dimensions and inflation," *Int. J. Mod. Phys. D* **16** (2007) 219–229, arXiv:hep-th/0602187.

[54] J. Sainio, "PyCOOL - a Cosmological Object-Oriented Lattice code written in Python," *JCAP* **04** (2012) 038, arXiv:1201.5029 [astro-ph.IM].

[55] Z. Huang, "The Art of Lattice and Gravity Waves from Preheating," *Phys. Rev. D* **83** (2011) 123509, arXiv:1102.0227 [astro-ph.CO].

[56] http://cosmo.kenyon.edu/gabe.html.

[57] R. Easther, H. Finkel, and N. Roth, "PSpectRe: A Pseudo-Spectral Code for (P)reheating," *JCAP* **10** (2010) 025, arXiv:1005.1921 [astro-ph.CO].

[58] G. N. Felder and I. Tkachev, "LATTICEEASY: A Program for lattice simulations of scalar fields in an expanding universe," *Comput. Phys. Commun.* **178** (2008) 929–932, arXiv:hep-ph/0011159.

[59] M. Patra and M. Karttunen, "Stencils with isotropic discretization error for differential operators," *Numerical Methods for Partial Differential Equations* **22** (07, 2006) 936 – 953.

[60] A. V. Frolov, "DEFROST: A New Code for Simulating Preheating after Inflation," *JCAP* **11** (2008) 009, arXiv:0809.4904 [hep-ph].

[61] B. Fornberg, "Generation of finite difference formulas on arbitrarily spaced grids," in *Numerical Modeling of Seismic Wave Propagation: Gridded Two-way Wave-equation Methods.* Society of Exploration Geophysicists, 01, 2012.

[62] D. G. Figueroa, J. Garcia-Bellido, and A. Rajantie, "On the Transverse-Traceless Projection in Lattice Simulations of Gravitational Wave Production," *JCAP* **11** (2011) 015, arXiv:1110.0337 [astro-ph.CO].

[63] J. Garcia-Bellido, D. G. Figueroa, and A. Sastre, "A Gravitational Wave Background from Reheating after Hybrid Inflation," *Phys. Rev. D* **77** (2008) 043517, arXiv:0707.0839 [hep-ph].

[64] S. Antusch, F. Cefala, D. Nolde, and S. Orani, "Parametric resonance after hilltop inflation caused by an inhomogeneous inflaton field," *JCAP* **02** (2016) 044, arXiv:1510.04856 [hep-ph].

[65] **LIGO Scientific, Virgo** Collaboration, B. P. Abbott *et al.*, "GW150914: Implications for the stochastic gravitational wave background from binary black holes," *Phys. Rev. Lett.* **116** no. 13, (2016) 131102, arXiv:1602.03847 [gr-qc].

[66] P. Amaro-Seoane, H. Audley, S. Babak, J. Baker, E. Barausse, P. Bender, E. Berti, P. Binetruy, M. Born, D. Bortoluzzi, J. Camp, C. Caprini,

V. Cardoso, M. Colpi, J. Conklin, N. Cornish, C. Cutler, K. Danzmann, R. Dolesi, L. Ferraioli, V. Ferroni, E. Fitzsimons, J. Gair, L. G. Bote, D. Giardini, F. Gibert, C. Grimani, H. Halloin, G. Heinzel, T. Hertog, M. Hewitson, K. Holley-Bockelmann, D. Hollington, M. Hueller, H. Inchauspe, P. Jetzer, N. Karnesis, C. Killow, A. Klein, B. Klipstein, N. Korsakova, S. L. Larson, J. Livas, I. Lloro, N. Man, D. Mance, J. Martino, I. Mateos, K. McKenzie, S. T. McWilliams, C. Miller, G. Mueller, G. Nardini, G. Nelemans, M. Nofrarias, A. Petiteau, P. Pivato, E. Plagnol, E. Porter, J. Reiche, D. Robertson, N. Robertson, E. Rossi, G. Russano, B. Schutz, A. Sesana, D. Shoemaker, J. Slutsky, C. F. Sopuerta, T. Sumner, N. Tamanini, I. Thorpe, M. Troebs, M. Vallisneri, A. Vecchio, D. Vetrugno, S. Vitale, M. Volonteri, G. Wanner, H. Ward, P. Wass, W. Weber, J. Ziemer, and P. Zweifel, "Laser interferometer space antenna," 2017.

[67] G. Cabass, L. Pagano, L. Salvati, M. Gerbino, E. Giusarma, and A. Melchiorri, "Updated constraints and forecasts on primordial tensor modes," *Phys. Rev. D* **93** (Mar, 2016) 063508. https://link.aps.org/doi/10.1103/PhysRevD.93.063508.

[68] M. A. Amin and Z.-G. Mou, "Electromagnetic Bursts from Mergers of Oscillons in Axion-like Fields," arXiv:2009.11337 [astro-ph.CO].

[69] M. Amin, "Smashing solitons of cosmology." https://www.youtube.com/watch?v=6GG2RjMwCUs&t=0s.

[70] S. Kawamura *et al.*, "Current status of space gravitational wave antenna DECIGO and B-DECIGO," arXiv:2006.13545 [gr-qc].

[71] P. Micikevicius, "3d finite difference computation on gpus using cuda," in *Proceedings of 2nd Workshop on General Purpose Processing on Graphics Processing Units*, GPGPU-2, p. 79–84. Association for Computing Machinery, New York, NY, USA, 2009. https://doi.org/10.1145/1513895.1513905.

Acknowledgement

Firstly, I would like to express my sincere gratitude to my advisor Prof. Laura Covi for continuously supporting me throughout the making of this thesis. It was always a great pleasure to consult her since her guidance would bring me new insights and steer me in the right direction, if needed. I would also like to thank Prof. Jens Niemeyer for offering his time to be the second referee. Additional thanks go to Felix Brüll from TU Clausthal for helpful discussions on code optimization.

Last but not least, I would like to thank my family and friends for always supporting me.

Erklärung Ich versichere hiermit, dass ich die vorliegende Arbeit ohne fremde Hilfe selbstständig verfasst und nur die von mir angegebenen Quellen und Hilfsmittel verwendet habe. Wörtlich oder sinngemäß aus anderen Werken entnommene Stellen habe ich unter Angabe der Quellen kenntlich gemacht. Die Richtlinien zur Sicherung der guten wissenschaftlichen Praxis an der Universität Göttingen wurden von mir beachtet. Eine gegebenenfalls eingereichte digitale Version stimmt mit der schriftlichen Fassung überein. Mir ist bewusst, dass bei Verstoß gegen diese Grundsätze die Prüfung mit nicht bestanden bewertet wird.

Göttingen, den March 15, 2021

(Robin Fynn Diedrichs)